Design and fabrication of a paraffin hybrid rocket engine

(versão após defesa)

Gonçalo Freire Pires Bidarra de Almeida

Dissertação para obtenção do Grau de Mestre em

Engenharia Aeronáutica

(Mestrado Integrado)

Orientador: Prof. Doutor Francisco Miguel Ribeiro Proença Brójo

Agosto de 2025

Declaração de Integridade

Eu, Gonçalo Freire Pires Bidarra de Almeida, que abaixo assino, estudante com o número de inscrição 44317 de/o Engenharia Aeronáutica da Faculdade de Engenharia, declaro ter desenvolvido o presente trabalho e elaborado o presente texto em total consonância com o **Código de Integridades da Universidade da Beira Interior**.

Mais concretamente afirmo não ter incorrido em qualquer das variedades de Fraude Académica, e que aqui declaro conhecer, que em particular atendi à exigida referenciação de frases, extratos, imagens e outras formas de trabalho intelectual, e assumindo assim na íntegra as responsabilidades da autoria.

Universidade da Beira Interior, Covilhã 25 /08 /2025

(assinatura conforme Cartão de Cidadão ou preferencialmente

assinatura digital no documento original se naquele mesmo formato)

Resumo

Esta dissertação apresenta o projeto, a construção e o teste experimental de um motor foguete híbrido à base de parafina, utilizando óxido nitroso como oxidante. O objetivo do projeto foi avaliar o comportamento da regressão do combustível de parafina em condições realistas e analisar o desempenho global do sistema. O motor apresenta uma configuração de grão cilíndrico único e foi testado sem técnicas de melhoramento da combustão. A taxa de regressão média medida foi de aproximadamente 1,0 mm/s, consistente com os valores registados para sistemas à base de parafina não aumentados. O consumo de combustível foi uniforme ao longo do comprimento do grão e a superfície queimada apresentou texturas onduladas caraterísticas dos combustíveis liquefeitos, indicando uma atividade de arrastamento limitada.

O sistema de alimentação do oxidante constituiu uma limitação significativa do desempenho. Enquanto as simulações termoquímicas baseadas numa relação O/F de 6,8 previam um desempenho ótimo, os testes reais revelaram um caudal de oxidante muito inferior (~57 g/s), resultando numa relação O/F medida mais próxima de 2,25. Esta discrepância foi atribuída a problemas de vaporização causados por um dimensionamento inadequado do injetor, por absorção de calor em componentes metálicos e por uma orientação do tanque que favoreceu a absorção de óxido nitroso na fase de vapor. O baixo fluxo de massa do oxidante contribuiu diretamente para a modesta taxa de regressão observada.

Apesar destas limitações, o projeto revelou conhecimentos valiosos sobre o desenvolvimento de foguetes híbridos em fase inicial, em particular a importância de alinhar os pressupostos do projeto com as limitações práticas do fluxo e as considerações térmicas. Os melhoramentos futuros devem centrar-se na otimização da área do injetor, na redução das perdas de pressão no sistema de alimentação, na garantia de uma extração adequada do líquido do tanque do oxidante e no potencial aumento da pressão da câmara através da modificação do bocal. Estas alterações têm como objetivo permitir um maior fluxo de massa de oxidante, melhorar o feedback térmico e atingir taxas de regressão mais representativas dos sistemas de propulsão híbridos de elevado desempenho.

Palavras-chave

Design; fabricação; motor foguete híbrido; parafina; oxido nitroso.

Abstract

This dissertation presents the design, construction, and experimental testing of a paraffin-based hybrid rocket motor using nitrous oxide as the oxidiser. The project's goal was to evaluate the regression behaviour of paraffin fuel under realistic conditions and analyse the system's overall performance. The motor featured a single cylindrical grain configuration and was tested without swirl or combustion enhancement techniques. The average regression rate measured was approximately 1.0 mm/s, consistent with values reported for unaugmented paraffin-based systems. Fuel consumption was uniform along the grain length, and the burned surface exhibited wave-like textures characteristic of liquefying fuels, indicating limited entrainment activity.

A significant performance limitation came from the oxidiser feed system. While thermochemical simulations based on an O/F ratio of 6.8 predicted optimal performance, actual tests revealed a much lower oxidiser flow rate (~57 g/s), resulting in a measured O/F ratio closer to 2.25. This discrepancy was attributed to vaporisation issues caused by inadequate injector sizing, heat soak into metallic components, and tank orientation that favoured the drawing of nitrous oxide in the vapor-phase. The low oxidiser mass flux contributed directly to the modest regression rate observed.

Despite these limitations, the project showed valuable insights into early-stage hybrid rocket development, particularly the importance of aligning design assumptions with practical flow limitations and thermal considerations. Future improvements should focus on optimising injector area, reducing pressure losses in the feed system, ensuring proper liquid draw from the oxidiser tank, and potentially increasing chamber pressure through nozzle modification. These changes aim to enable higher oxidiser mass flux, enhance thermal feedback, and achieve regression rates more representative of high-performance hybrid propulsion systems.

Keywords

Design; fabrication; hybrid rocket engine; paraffin; nitrous oxide.

Table of Contents

List of Figures

List of Tables

List of Acronyms

AN	**Ammonium Nitrate**
AP	**Ammonium Perchlorate**
ARPA	**Advanced Research Projects Agency**
ASA	**Acrylic Styrene Acrylonitrile**
CAD	**Computer-aided Design**
CEA	**Chemical Equilibrium Analysis**
DARPA	**Defense Advanced Research Projects Agency**
DAS	**Data Acquisition System**
F/O	**Fuel to Oxidiser ratio**
FLOX	**Fluorine/Oxygen mixture**
GOx	**Gaseous oxygen**
HRE	**Hybrid Rocket Engine**
HTPB	**Hydroxyl-terminated polybutadiene**
HV	**Hardness Value**
ICS	**Ignition Control System**
IF1	**Injector Fixation component one**
IF2	**Injector Fixation component two**
IRFNA	**Inhibited Red Fuming Nitric Acid**
JP	**Jet Propellant**
LoRa	**Long Range**
LOX	**Liquid Oxygen**
LRE	**Liquid Rocket Engine**
MON	**Mixed Oxides of Nitrogen**
NASA	**National Aeronautics and Space Administration**
NF1	**Nozzle Fixation component one**
NF2	**Nozzle Fixation component two**
O/F	**Oxidiser to fuel ratio**
PB	**Polybutadiene**
PCB	**Printed Circuit Board**
PE	**Polyethylene**
SRM	**Solid Rocket Motor**
U.S.	**United States**
UTC	**United Technology Center**

List of Symbols

$\dot{m}_f$	Fuel mass flow rate	[kg/s]
$\dot{m}_{ox}$	Oxidiser mass flow rate	[kg/s]
$\dot{m}_{SPI}$	Mass flow rate under single-phase incompressible liquid flow	[kg/s]
$\dot{m}_t$	Total mass flow rate	[kg/s]
m_{ox}	Oxidiser mass	[kg]
$\dot{r}$	Regression rate	[mm/s]
A_2	Area of a single injector orifices	[mm^2]
A_c/A_t	Combustion chamber to throat area ratio	
A_t	Throat area	[mm^2]
A_{total}	Total area of the injector orifices	[mm^2]
A_{wf}	Wetted fuel surface area	[mm^2]
b_t	Burn time	[s]
C_d	Discharge coefficient	
D_i	Internal diameter of the fuel grain	[mm]
d_t	Throat diameter	[mm]
f	Safety factor	
G	Local mass flux through the port	[kg/s*m^2]
γ	Gamma	
G_{ox}	Mass flux of oxidiser through the port	[kg/s*m^2]
$h_{(t,min)}$	Minimum thickness	[mm]
I_{sp}	Specific Impulse	[s]
L	Length of fuel grain	[mm]
L/D	Length to diameter ratio of the fuel grain	
m_f	Fuel mass	[kg]
n	Oxidiser mass flux exponent coefficient	
N	Number of injector orifices	
P_c	Combustion chamber pressure	[bar]
P_t	Throat pressure	[bar]
R	Perfect gas constant	[J/kg*K]
T_t	Throat temperature	[K]
V_f	Volume of fuel	[mm^3]
ΔP	Pressure differential across the injector	
ρ_f	Density of the fuel	[kg/mm^3]

σ_{yield}	**Yield strength**	**[N/m^2]**
a	**Regression rate coefficient**	

Chapter 1 – Introduction

1.1. Motivation

Among the propulsion systems available, hybrid rocket motors have received some interest due to their potential benefits in terms of safety, cost-effectiveness and versatility.

Traditional solid rocket motors and liquid rocket engines have each demonstrated their own strengths and weaknesses. SRMs provide simplicity and high thrust-to-weight ratios but lack throttle-ability and the ability to be shut down once ignited is possible but adds complexity to the system. LREs allow precise thrust control and the capability to be restarted, but their complex plumbing and risk of catastrophic failure present considerable challenges. Hybrid rocket motors attempt to fill this gap by combining the simplicity and safety of SRMs with some of the controllability characteristics of LREs.

Hybrid rocket motors, with independent fuel and oxidiser systems, reduce the chance of inadvertent ignition and catastrophic failure. The nature of hybrid propulsion systems allows for safer handling, shipping, and storage, making them desirable for a variety of applications such as space tourism, satellite deployment, and scientific missions [1].

The allowed simplicity of hybrid rocket designs, simplifies manufacturing processes and reduces production costs. With fewer moving parts and less complex infrastructure requirements compared to LREs, hybrid rocket motors offer a more economical solution for propulsion needs across a multitude of applications.

In an era increasingly concerned with environmental sustainability, paraffin, a commonly available and inexpensive hydrocarbon wax, serves as an attractive fuel option for hybrid motors. The combustion of paraffin and nitrous oxide produces relatively benign by-products compared to the toxic and environmentally harmful emissions associated with conventional solid and liquid propellants [2].

Furthermore, the use of non-toxic propellants simplifies handling procedures and reduces the need for extremely strict safety measures.

Hybrid rocket engines also offer an opportunity for students to handle liquid propellants while being relatively safe and easier to operate compared to liquid bi-propellant engines.

1.2. Objectives

The main goal with this project was the design, fabrication and testing of a hybrid rocket motor, utilising paraffin as fuel and nitrous oxide as oxidiser. This motor was meant to be simple and interchangeable, meaning that with relatively simple alterations and/or with the manufacturing of new components, allow for different versions to be tested. These changes are mainly in the injector plate design and nozzle.

It is also worth mentioning the objective of incorporating a nozzle made by another student.

1.3. Structure of the dissertation

This dissertation is organised into chapters and subdivisions, beginning with Chapter 2 with a literature review followed by the state of the art, where hybrid rocket engines will be compared to solid rockets and liquid bipropellant rockets, where their advantages and disadvantages will be discussed. Then paraffin and nitrous oxide are investigated as hybrid rocket fuel and oxidiser, respectively.

In Chapter 3 the methodology is shown, starting with the nozzle dimensions, followed by the analysis performed with the Chemical Equilibrium with Applications software, resulting in the dimensions and geometry of the fuel grain, combustion chamber and injector plate.

In Chapter 4, all the fabrication processes are shown and explained and the subsequent hardening processes of some of the components. Every system required for the testing of the engine is explained, such as the feeding system, ignition system and the control and data acquisition systems. This chapter finishes with the implementation of such systems and a final, simple preliminary test.

In Chapter 5, it’s the discussion of the results obtained from the tests. Following in Chapter 6 are the final considerations, including the conclusions and future works.

Chapter 2 - Literature review

2.1. The history of hybrid rockets

Early history (1933-1960)

GIRD-9 from the Soviet Union, in 1933, designed by Mikhail K. Tikhonravov and Sergei P. Korolev, with approximately 0,18 m in diameter and 2,44 m long, achieved a thrust of 500 N for 15 s, an altitude of 1,500 m using liquid oxygen and gelled gasoline. Ever since, many combinations of fuels and oxidisers have been experimented.

The first significant effort of a capable hybrid rocket was conducted in the 1940s by the Pacific Rocket Society which experimented with liquid oxygen with fuels such as wood (Douglas fir), wax loaded with carbon black, and a rubber-based fuel. The Douglas fir rockets, tested in 1947, were designated XDF-#. The two initial recorded configurations, XDF-3 and XDF-4, used a nozzle made of Douglas fir, XDF-3 was soaked in a solution of zinc and ammonium chlorides, while the XDF-4 wood nozzle contained a thick moulded lining of calcium sulfate. The XDF-3 nozzle design failed when 15 seconds of low-pressure combustion destroyed the nozzle while the XDF-4, after 2 s of firing time, the static test motor broke away from the test stand, showing that a correct evaluation of the design was not made, a thrust of 178-267 N was reached, higher than the one of the stand, flying over the heads of the observers landing under a Jeep parked nearby. XDF-23, containing a LOX rubber-base fuel and an aluminium alloy nozzle, successfully flew in June 1951, reaching an estimated altitude of 9150 m [2].

Despite the Society not reporting any ballistic analysis, they had an accurate concept of hybrid burning as shown by the following statement: "The chamber pressure of a solid–liquid rocket engine is proportional to oxidiser flow and not to the internal surface area exposed to the flame. Thus, there is no danger of explosions due to cracks and fissures in the charge, as with solid propellant rockets commonly used for boosters" [3].

The throttleability and safety of these types of engines were recognised early.

From the late 1940s to 1956, *George Moore* and *Kurt Berman* conducted an analytical and experimental investigation at General Electric Company using polyethene as fuel and hydrogen peroxide as the oxidiser, having as the objective of the analysis to increase the performance of hydrogen peroxide (H_2O_2) as a monopropellant [4].

It was proved that when a relatively small amount of fuel was added, around 15% of the propellant weight, there was an increase of 70% in the I_{sp}. It was concluded by the authors that longitudinal uniformity was exceptional, cracks in the grain did not affect the combustion, hard starts were not observed, combustion was stable because the fuel surface was acting as its own flame holder, throttling was easy with a single valve, and a high liquid-to-solid ratio was desirable to simplify uniform burning in the combustion chamber, and a problem with the thermal instability of H_2O_2 was noted. The authors' observations and conclusions were largely substantiated in the following years [3].

William Avery and coworkers at the Applied Physics Laboratory of Johns Hopkins University in 1952 did burning tests with a reverse hybrid rocket configuration. The main focus was on JP and ammonium nitrate because they were one of the available propellants with the lower cost, which was the main objective of the investigation. This combination of propellants proved to be difficult to burn. The problems were rough burning and poor performance. The liquid-to-solid ratio (F/O) of this propellant combination is in the range of 0.035, about 200 times smaller than what Moore and Berman used [3].

The reverse hybrid concept was also studied by both Thiokol and United Technology Centre in the 1960s using hydrazine-based liquid fuels and solid oxidisers such as ammonium perchlorate, hydrazinium diperchlorate, and nitronium perchlorate. Future endeavours were dismissed due to poor combustion behaviour and insufficient improvement in performance [3].

Enlightenment era

In the 1960s, there was an increasing interest in hybrid propulsion by the U.S. Military Forces, such as the U.S. Army, Navy and Air Force and the Advanced Research Projects Agency (ARPA, currently having a 'D' that stands for Defence, DARPA) sponsored around 40 research projects. Some U.S. companies also started research with their own funds. The biggest contributor was the UTC group, which ended up responsible for developing the solid rocket boosters for the Titan vehicle.

In 1959, shortly after the creation of the UTC, David Altman started to assemble a group to investigate the fundamentals of hybrid combustion, which led to several experiments during the 1960s. A wide variety of fuels and oxidisers were studied, such as IRFNA, N_2O_4, MON, FLOX, O_2, and air as oxidisers and the various PBs with such additives as Al, Mg, Li, AP, and AN [3].

The development of the hybrid demonstrator in 1960 allowed for a safe and low-cost laboratory-scale tool to investigate the combustion mechanisms of hybrid propellants.

In 1961, Marxman and Gilbert developed the first hybrid regression rate equations [5].

Considerably the best accomplishment of that era was the development of a regression rate model, by Marxman in 1963, that was based on schlieren photographs taken by Muzzy, and which showed both momentum and combustion layers, the impact of blowing on reducing the heat flux, the use of a total effective heat of vaporisation to account for various thermal reactions at the surface and the contribution of radiation when coupled with convection [6].

According to Chiaverini and Kuo in 2007, this model is so complete that it is still being used [7].

The years to follow were not as impressive in terms of scientific development, since the focus was on the development of the motors, improvements in the regression rate models, throttling transients and hypergolic fuels [8].

Recent Advances

Interest in designing a large-size rocket booster increased since the Challenger disaster in 1986, when NASA started to sponsor the replacement of solid rocket boosters with hybrid boosters. In the 1980's Hydroxyl-Terminated-Polybutadiene (HTPB) was beginning to be tested as a fuel in hybrid sounding rockets. In the late-1990s, the biggest problem of the large-scale hybrid rockets was their low regression rate due to the diffusive nature of the combustion process [9].

Real attempts to increase the regression rates started in the 1960s, using energetic fuel additives, such as ammonium perchlorate (AP) [NH_4ClO_4] and ammonium nitrate (AN) [NH_4NO_3]. They were named liquid augmented solid propellants, but there is a critical concentration for which the fuel acts as a low-grade propellant, becoming explosive. Other additives were tested, but even though effective in most cases, the method increased risk compared to conventional hybrids, hence increasing costs [3].

Designs with high turbulence conditions at the surface of the burning fuel were also investigated, with the intent to increase the heat transfer coefficient. Per example, adding an easily vaporisable component that creates cavities to uneven the surface during its vaporisation. There was also the use of crystalline additives, as did Boardman in 1997, with swirling injectors or injection at the aft end of the chamber, as did by Knuth in 1998, Yuasa in 2001, Knuth in 2002, Lee in 2005. Caravella tested an end-burning hybrid motor that used radial flow injectors to burn PE fuel with decomposed H_2O_2. Metal particles were also tested as an additive to the solid fuel. In 2002, Risha conducted a series of experiments with HTPB based fuels and nanoparticles of aluminium, achieving higher regression rate values than the pure HTPB [10], [11], [12], [13], [14], [15] ,[16].

2.2. State of art

2.2.1. Hybrid propulsion

Hybrid rockets are a combination of solid and liquid motors, adopting characteristics of both. Having as the most common combination the fuel in the solid phase and the oxidiser in the liquid phase.

Solid rocket motors consist of fuel and oxidiser pre-mixed into a single propellant grain. Liquid rocket engines comprise of fuel and oxidiser, usually cryogenic and at low pressures, in the liquid phase [7].

Figure 1 illustrates the configurations of the three types of rocket engines.

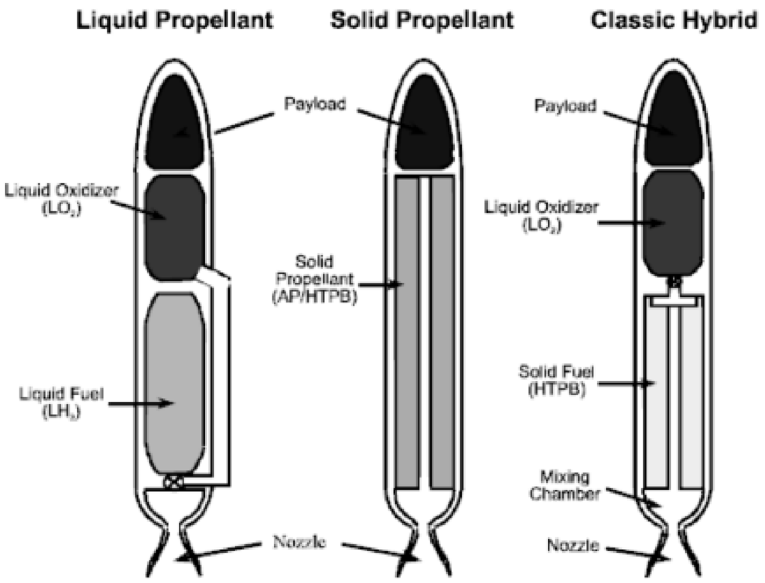

Figure 1 - Three types of chemically-powered rockets [7].

The hybrid rocket engine has two separated propellants, one in the solid state, typically the fuel grain, and the oxidiser in gas or liquid state, this is the classical configuration. Shortly after ignition, through the injection of the oxidiser into the fuel grain port, its combustion with the fuel pyrolysis products generates a macroscopic diffusion flame, which sustains the fuel grain pyrolysis and regression of the fuel grain process via convective and radiative heat transfer. Figure 2 shows the schematic of the combustion process [17].

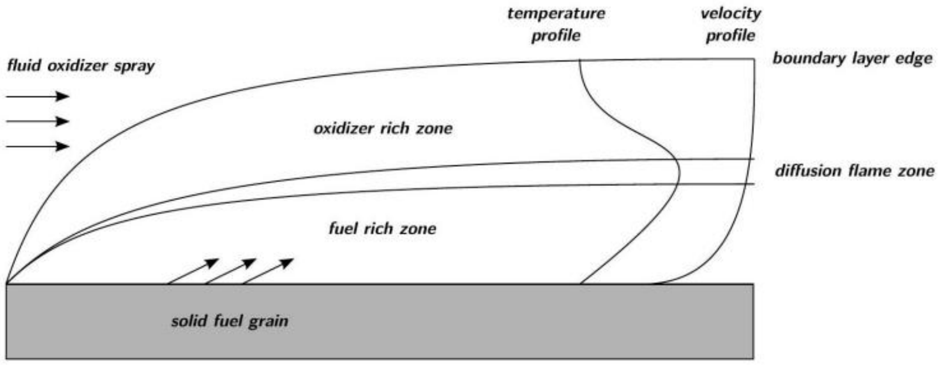

Figure 2 - Hybrid rocket engine combustion schematic [18].

This technology can be applied in boosters and upper stages of launch vehicles, in addition to tourism spacecrafts and satellite orbital manoeuvres. All these missions have common requirements, such as thrust control, capability of multiple ignitions and non-toxic propellants that need to be stored for a long time.

The main advantages of hybrid propulsive systems involve their simple design and safe operation. In addition, it is possible to obtain specific impulses greater than in solid systems and perform ignition and thrust control, if necessary. However, the increasing inner radius of the fuel grain during combustion, results in a variation in the propellant mixing ratio, if the oxidiser flux is kept constant or during throttling. Since the oxidiser mass flux can be controlled so is the engines thrust [19].

The low regression rate of the solid fuel grain, and combustion instabilities are disadvantages that characterise a hybrid rocket engine.

The regression rate, which has an important role in the hybrid rocket development, has a relation with the oxidiser mass flux, and not with the combustion chamber pressure like in the solid rockets, making this a less susceptible engine to explosion and having the combustion chamber pressure as a free parameter that can be designed for the mission of interest [20].

Advantages of hybrid rockets

Paraffin-based fuels have a natural attribute of a high regression rate, not requiring the need for oxidizing additives or other regression rate enhancers, who are usually responsible for compromising safety and increased costs. These fuels provide specific impulse performance comparable to kerosene whilst being approximately 17% denser, allowing for a higher volumetric loading, single-port design system, with a density impulse comparable to or greater than a hydrocarbon fuelled liquid system [20].

The density impulse uses the density of the propellants to measure the obtained impulse from a given volume of propellant, a higher density propellant packs more propellant into a smaller volume, so it has a higher impulse density because that is the measure of specific impulse per volume. The specific impulse is defined as the total impulse produced for a given propellant weight or the efficiency of a rocket using a particular propellant. [21]

This higher regression rate removes the need of a complex multiport configuration, as represented in Figure 3.

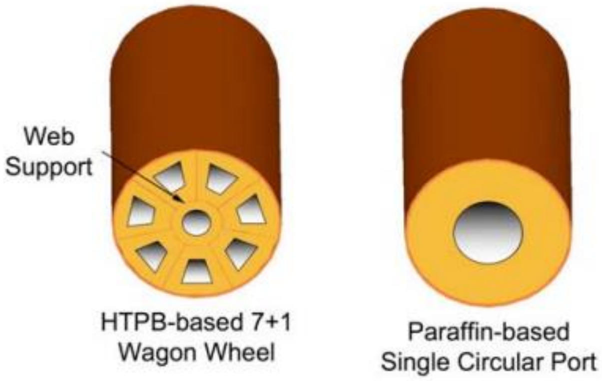

Figure 3 - Multiport vs single-port grain configuration [20].

A series of scale-up tests at Standford University using a variety of oxidisers such as gaseous oxygen, liquid oxygen, and nitrous oxide were performed by B. Cantwell, A. Karabeyoglu, and D. Altman revealing that the data from these testes were in agreement with the small-scale, low-pressure, and low-mass-flux laboratory tests and confirm the high regression rate behaviour of the fuel at chamber pressures and mass fluxes present in commercial applications [20].

Comparison to solid rockets

The reason why the two basic types of chemical rocket propulsion exhibit hazardous operation comes mainly from the oxidiser and fuel that must mix to release energy in the combustion chamber. In solid propellant rockets, the fuel and oxidiser are already mixed and bound through a polymer binder. Cracks and/or imperfections in the propellant geometry can cause an uncontrollable combustion and in some cases explosion.

Whilst the hybrid rocket concept has been known for over 85 years it was not given considerable attention until the 1960s. Its nonexplosive nature was the main reason for interest, safety in both operation and manufacture, allowing for the fuel to be fabricated at any conventional commercial site and even at the launch site with no danger of explosion. Hence grandly reducing costs of manufacture and launch operation.

Hybrids also offer a reduced sensitivity to cracks and debounds in the propellant, higher specific impulse, throttle-ability and the ability to terminate/restart thrusting when desired.

The combustion products are relatively environmentally benign when compared with conventional solids that usually rely on perchlorate-based oxidisers. The combustion products of solid rockets contain acid-forming gases such as hydrogen chloride. There is also the concern about the effects of low levels of environmental perchlorate, which comes mainly from the explosive and propellant manufacture [20], [22].

Comparison to liquid bipropellant rockets

Liquid bipropellant rockets represent a higher explosion hazard than hybrid rockets, since an intimate mixture of oxidiser and fuel is not possible on the latter. Also, only requiring one instead of two liquid storage and delivery systems and allowing for a reduced complexity with the omission of a regenerative cooling system for both the chamber and nozzle.

Control over the throttle is simpler since it is not required to match the momenta of the two propellant streams during throttling.

The theoretical specific impulse of hybrid rockets is comparable to a bipropellant liquid since the oxidisers are the same, and the solid fuels are hydrocarbons with energy content identical to kerosene. However, hybrid solid fuels have the advantage of having their densities typically 15–20% greater than the density of liquid kerosene.

One of the main advantages of hybrids over bipropellant liquids is the ability to add energetic materials. Since the fuel is in the solid state, adding performance-enhancing materials such as aluminium powder is very easy. The heat of reaction provided by the addition of aluminium is sufficient to counteract the increase in molecular weight of the combustion products, resulting in a small increase in I_{sp}, depending on the oxidiser. The biggest benefit associated with the addition of aluminium is the considerable increase in fuel density compared to a hydrocarbon fuelled liquid system. There is also a very interesting consequence that occurs when adding aluminium to storable oxidisers like N_2O_4, in which the fuel tends to both increase the theoretical I_{sp} and shift the peak I_{sp} to lower values of the oxidizes to fuel (O/F) ratio. For the same mass of propellant, there is a bigger portion of this denser solid propellant, resulting in a reduced liquid feed system, allowing better performance [20].

2.2.2. What's the problem with hybrids?

Even though the concept of HREs has been known since the initial investigations on solid and liquid rockets, they have only been used for suborbital flights thus far. A cause for this is most likely the difficult process required to completely understand the physics behind their operations. In fact, hybrid rocket propulsion involves multiple coupled phenomena, such as combustion, convection, radiation, and pyrolysis, as well as inherent disadvantages, such as the shifting of the mixture ratio and the infamous low regression rate of the fuel grain, as well as potential drawbacks, such as poor combustion efficiency and low frequency combustion instability. To achieve a comprehensive and general understanding of a single phenomenon and its couplings, and allow feasible solutions, some difficult modelling issues must be overcome, as well as strict collaboration of experiments with theoretical and numerical activities. This has historically favoured the solid and liquid rockets, slowing HRE maturation [23].

The major disadvantages associated with hybrids are:

There are a few disadvantages associated with hybrids, such as their low combustion efficiencies (93-98%), which are slightly lower than those of liquid-propellant or solid-propellant rockets. Fuel is prone to remain in the combustion chamber at the end of its operation, reducing the solid-fuel mass fraction. In comparison to solid-propellant rockets, hybrids usually have a lower density impulse, resulting in bigger volumes. The regression rates of the commonly used solid fuels in classical hybrids are low compared with solid propellants, imposing limitations on the design of the fuel grain.

There is also the variance in the oxidiser to fuel mass ratio during operation, resulting in variations of the I_{sp}.

It is clear that the hybrid-propulsion system has quite a few advantages (and not so many disadvantages) over existing solid-propellant and liquid-propellant propulsion systems.

An obvious question as to why hybrid rockets are not being used widely and have not been fully developed has to be raised. The following reasons could explain the current scenario.

1) Solid-propellant rockets are often launch-ready and simple to use, particularly for military applications.

2) Many battleships have restrictions on liquid oxidisers, making it difficult to deploy hybrid rocket-powered missiles.

3) From a performance standpoint, liquid-propellant rockets offer a high specific impulse, making them favoured for civil space launch purposes.

4) Experts in the chemical propulsion sector are split, with competence in either liquids or solids.

5) Scaling laws have not been fully studied for hybrid rockets.

6) Unlike the burning rate of solid propellants, the solid-fuel regression rate is dependent on a variety of factors. Historically, there has not been a basic understanding of the solid fuel combustion processes under either simulated or actual motor operating conditions. Usually, the support for the research portion of a hybrid program is a very small fraction of the overall motor development program. Since there is a lack of financial support, research studies are usually conducted in very narrow scopes.

7) There is a scarcity of long-term national initiatives and international collaborative activities in the development of hybrid rockets. However, this trend is predicted to shift due to several appealing aspects of hybrid rockets [7].

2.2.3. Paraffin waxes as hybrid rocket fuel

Hybrid rocket engines (HREs) have regression rates around 1 mm/s, values about ten times smaller than those of solid rocket motors (SRMs). There is also the fact that SRMs regression rate is dependent on the chamber pressure, whilst the regression rate of HREs is mainly dependent by the local mass flux through the port G, according to Marxman's theory [6], [24].

$$\dot{r} = aG^n x^m \ [17]$$

(2.1)

a being a constant that depends on the combination of propellants and the turbulence level, and n an exponent with values typically ranging from 0.6 to 0.8. Equation 2.1 is, for the most part, often used in a simpler form by assuming the regression rate is independent of the longitudinal location along the port, resulting in a ballistic coefficient of $\mathrm{m} = 0$. The finished form of this estimation is the most commonly used classical hybrid regression rate law that now relates to the mass flux of oxidiser through the port, G_{ox}.

Amongst the disadvantages of HREs, the most significant is the low regression rate since it impedes reaching high thrust levels in the optimum O/F ratios. Attempts to overcome this problem have been made, multi-port grains allowing a large, wetted surface have been used to increase the fuel mass flow rate to compensate for the low regression rates. This leads to poor volumetric loadings and unwanted fuel slivers [17].

Through swirl injection, a seven times increase in the regression rate was achieved; however, maintaining a high level of swirl through the length of the port and scaling this approach has proven to be very difficult [2]. An attempt to make the regression rate sensitive to the chamber pressure, a characteristic from SRMs, an oxidising agent like ammonium perchlorate has been added to the fuel grain. However, this approach removes the associated safety and environmental advantages of the hybrid rocket. A different technique was tried, increasing the heat transfer toward the fuel grain, this was found to be unsuccessful because of a blocking effect. Even though the rate of pyrolysis increases by increasing the wall heat transfer, the increase in mass flux from the surface tends to reduce the wall temperature gradient, limiting the heat transfer itself [20]. In the 1990's cryogenic fuels were given attention by multiple research groups. Carrick and Larson, De Rose et al., Clair et al., and Gramer et al. made several tests with cryogenic hydrocarbons, mainly methane and pentane, resulting in some regression rates ten times higher than those of classical polymeric fuels [25], [26], [27], [28].

Karabeyoglu et al., after many experiments and analysis, developed a mathematical model explaining such strange behaviour. It was shown that this increase in regression rate was justified by the formation of a hydrodynamically unstable melt layer above the grain surface, entraining fuel droplets into the fuel grain port. This mechanism of an additional mass transfer into the port acted as a continuous spray along the port, with most of the fuel pyrolysis occurring around droplets between the melt layer and the flame front, where there is a higher energy than at the wall interface, and no blocking effect occurs [20]. To begin, the existence of a melt layer was recognised and its linear stability under high shear stresses analysed. Then the melt layer instability was related to droplet entrainment through experimental results and semi–empirical correlations from film–cooling literature. Finally, Marxman's regression rate theory was expanded to liquefying fuels. The entrained mass flow rate was found to be dominant and directly proportional to dynamic pressure and melt layer thickness, while being inversely proportional to its dynamic viscosity and surface tension [29], [30]. Through the extension of the theory to non–cryogenic hydrocarbons, amongst normal alkanes that are solid at room temperature, paraffin waxes appeared, exhibiting the highest entrainment and thus expected to have the highest regression rates. Lab–scale firing tests were conducted at Stanford University using gaseous oxygen (GOX) as the oxidiser, where Karabeyoglu et al.'s predictions were confirmed. Regression rate values of the used fuel formulations of paraffin–wax were three to four times higher than those of pyrolysing fuels like hydroxyl–terminated polybutadiene (HTPB) [31]. There were also a series of scale-up tests performed in the NASA Ames hybrid combustion facility. These tests revealed data that agreed with the small–scale, low pressure and low mass flux laboratory tests performed at Stanford University, this confirmed that paraffin-based fuels were in fact high regression rate fuels. These tests were made at chamber pressures and mass fluxes typical of flight applications [32].

This newly discovered entrainment mechanism of paraffin–based fuels allowed high regression rates without compromising the characteristic simplicity and safety of HREs. This enabled the design of high volumetric loading single–port combustion chambers, not requiring the complex multi–port fuel grains. Paraffin-based fuels are also non–hazardous and environmentally benign; they also provide theoretical specific impulses higher than rockets fuelled by kerosene [20]. Paraffin–based HREs exhibit low combustion efficiencies, which can hinder the theoretical performances. There is also the change in O/F ratio and the tendency to low-frequency combustion instabilities. All these problems remain a point of attention that still need to be considered or further investigated. The paraffin–based fuel concept has reignited an interest in the hybrid rocket technology. A significant number of experiments and new numerical models, and simulations have been successful worldwide. Almost every year, research and development projects aimed at increasing technology readiness are planned, with growing engagement from private stakeholders.

2.2.4. Nitrous oxide as hybrid rocket oxidiser

Also known as dinitrogen monoxide or “laughing gas”, nitrous oxide is an odourless and colourless oxidiser that has been a very attractive choice for small scale hybrid rocket development due to its safety, handling, availability and relative low cost. It’s a great option due to its operational simplicity, non-toxicity and stability at room temperature.

At room temperature it is not flammable but supports combustion at elevated temperatures [19].

It is known for its exothermic decomposition where large amounts of energy are produced, making it a good choice in terms of theoretical I_{sp} performance and motor stability/efficiency, unfortunately it also represents a chemical explosion hazard. N_2O has a positive heat of formation and when above 520°C or when in contact with hydrogen or hydrocarbon vapor, can quickly decompose into N_2 and O_2 by releasing substantial heat [20], [33].

Nitrous oxide is a self-pressurising gas at atmospheric conditions, making it not require pumps or external pressurisation systems. It can also be safely stored at room temperature. These are the main reasons why it is used so much.

Even though it has a low theoretical specific impulse, it has a very high storage density. This means it can deliver a higher change in spacecraft velocity per unit volume of propellant. Denser propellants are preferred in small systems since they are volumetrically constrained.

Some scenarios and/or materials can make N_2O sensitive to shock. Reaching the supercritical state where, at 36°C, it becomes a supercritical fluid and therefore compressible. Interactions with hydrocarbons and iron oxide are also shock sensitive scenarios. Caution must be taken when designing a hybrid rocket system using nitrous oxide as the oxidiser. Contact with materials that are incompatible may result in explosions, serious caution should be taken in the selection and cleanness of the materials that will come in contact with the nitrous oxide [34].

The following list are safety recommendations when dealing with nitrous oxide propulsion systems:

- The surroundings of the test bench should be marked, and personnel should be at safe distances.

- Oxidiser tanks should be placed in a vertical arrangement, to ensure that there will always be a liquid layer separating the combustion chamber from the vapour from the tank's ullage.

- To prevent a build-up of nitrous oxide in the combustion chamber, the igniter should be switched on before the nitrous oxide flow is enabled.

- Careful cleaning procedures should be implemented.

- Components must be compatible with nitrous oxide, such as valves, O-rings, gaskets and any other material used [21].

Table 1 shows the properties of nitrous oxide and Table 2 shows the nitrous oxide compatibility chart.

Table 1 - Nitrous oxide properties [21].

Molecular Weight	Molecular weight:	44.013 g/mol
Solid Phase	Melting point:	-90.82 °C
	Latent heat of fusion (1.013 bar at melting point):	148.57 kJ/kg
Liquid Phase	Liquid density (1.013 bar at boiling point):	1230.458 kg/m^3
	Boiling point (1.013 bar):	-88.47°C
	Latent heat of vaporisation (1.013 bar at boiling point):	374.286 kJ/kg
	Vapour pressure (at 20°C):	50.525 bar
Critical Point	Critical temperature:	36.37°C
	Critical pressure:	72.45 bar
	Critical density:	452.011 kg/m^3
Gaseous Phase	Gas density (1.013 bar at boiling point):	2.982 kg/m^3
	Gas density (1.013 bar at 15°C):	1.8724 kg/m^3
	Compressibility factor (1.013 bar at 15°C):	0.99391
	Specific gravity:	1.53
	Specific volume (1.013 bar at 25°C):	0.553 m^3/kg
	Heat capacity at constant pressure (1.013 bar at 25°C):	0.0389 kJ/(kgK)
	Heat capacity at constant volume (1.013 bar at 25°C):	0.304 kJ/(kgK)
	The ratio of specific heats (1.013 bar at 25°C):	1.2804
	Viscosity (1.013 bar at 0°C):	13.631 µPas
	Thermal conductivity (1.013 bar at 0°C):	16.464 mW/mK

Table 2 - Nitrous oxide compatibility [21].

Material	Compatibility
Metals	
Aluminium	Satisfactory
Brass	Satisfactory but corrosive in presence of moisture
Copper	Satisfactory but corrosive in presence of moisture
Ferritic Steels	Satisfactory but corrosive in presence of moisture
Stainless Steels	Satisfactory
Plastics	
Polytetrafluoroethylene (PTFE)	Satisfactory
Polycholrotriflouroethylene (PCTFE)	Satisfactory
Vinylidene polyflouride (PVDF)	Acceptable but possible ignition under certain conditions
Polyamide (PA)	Acceptable but possible ignition under certain conditions
Polypropylene (PP)	Acceptable but possible ignition under certain conditions
Elastomers	
Buthyl (isobutene-isoprene) rubber (IIR)	Not recommended, possible ignition and significant swelling
Nitrile rubber (NBR)	Not recommended, possible ignition and significant swelling
Chloroprene (CR)	Not recommended, possible ignition and significant swelling
Chloroflourocarbons (FKM)	Not recommended, significant swelling
Silicon	Satisfactory
Ethylene-propylene (EPDM)	Not recommended, possible ignition and significant swelling
Lubricants	
Hydrocarbon-based lubricant	Not recommended, possible ignition
Fluorocarbon-based lubricant	Satisfactory

Chapter 3 – Methodology

In this chapter, the engine sizing process will be described, along with the materials utilised in its construction. Additionally, the fabrication process will be discussed. CAD drawings of the components can be found in Chapter 4.

3.1. Nozzle

Starting by evaluating the nozzle geometry (see Fig. 4, 5 and 6), which was fabricated by another student [35]. This assessment provided constraints, including the minimum combustion chamber diameter. Given that the throat diameter (d_t) is 8.1 mm, the minimum combustion chamber diameter is given by 8.1×4=32.4 mm. This was a wanted parameter so the pressure differential in the thrust equation could be neglected.

Figure 4 - Nozzle's isometric and side view.

Figure 5 - Nozzle's top and bottom view.

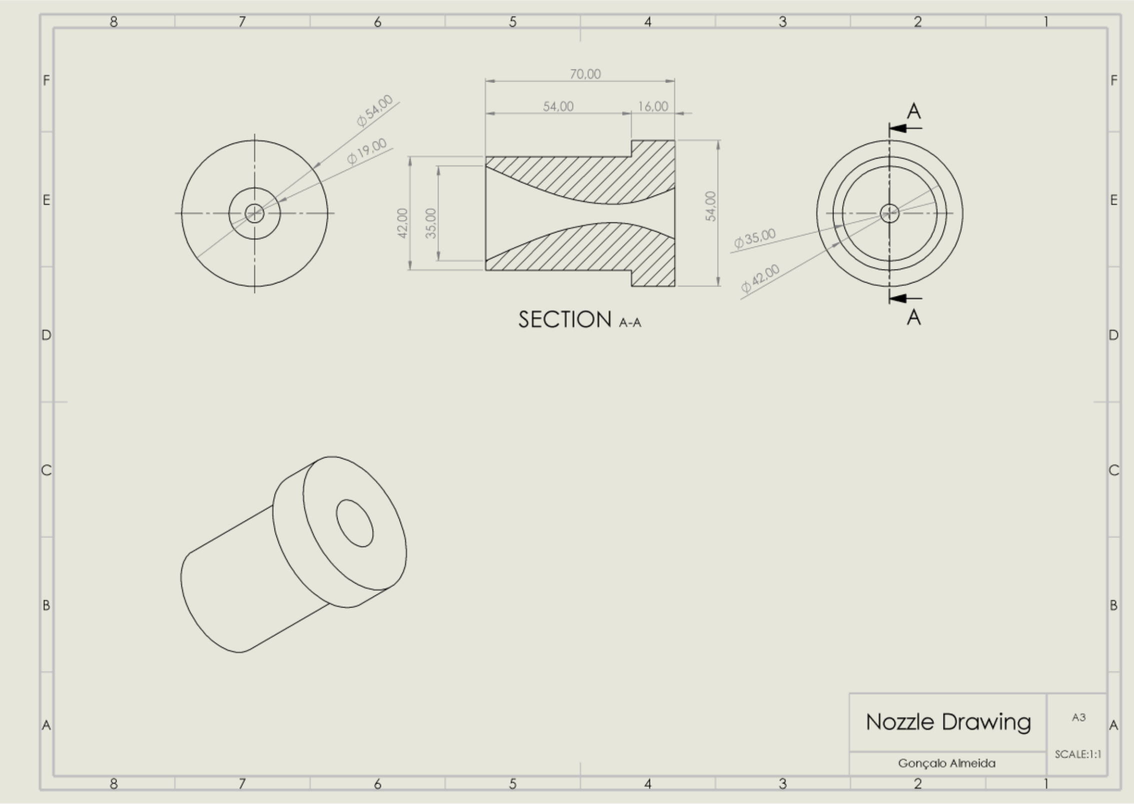

Figure 6 - Nozzle technical drawing.

3.2. CEA (Chemical Equilibrium with Applications)

The NASA CEA software required the contraction ratio (Ac/At) as an input parameter. However, this value had not been determined, since the internal diameter of the combustion chamber had not been established. A mechanical steel tube with an internal diameter of 54 mm and an external diameter of 60 mm was proposed, resulting in a contraction ratio of 44.44.

The next required parameter was the supersonic area ratio, which was determined to be 4.27 after evaluating the nozzle. With these values, along with the known combination of propellants, the analysis aimed at determining the optimum values for the engine could continue. Parameters such as the oxidiser-to-fuel (O/F) ratio, specific impulse (I_{sp}), temperature, and pressure were evaluated. To determine the optimal O/F ratio, the highest I_{sp} value was used as the determining criteria. Additionally, the exit pressure was considered to ensure it was close to atmospheric pressure. The highest I_{sp} value was obtained at an O/F ratio of 6.8 and an injection pressure of 26 bar. Although there was a very slight increase in I_{sp} with higher injection pressure, it was not significant enough to justify potential complications. Table 7 in Appendix A presents the output provided by NASA CEA.

3.3. Fuel grain geometry

With the values provided by NASA CEA, calculations for sizing the fuel grain could now begin. The following equations were used in the experimental calculations to determine the dimensions of the fuel grain.

The results of these calculations are presented in Table 8 in Appendix A.

Total mass flow rate, $\dot{m}_t$, where P_t, A_t, T_t are the pressure, area and temperature of the throat:

$$\dot{m}_t = \frac{P_t A_t}{\sqrt{T_t}} * \sqrt{\frac{\gamma}{R}} * \left(\frac{\gamma + 1}{2}\right)^{-\frac{\gamma+1}{2(\gamma-1)}}$$

(3.1)

Fuel mass flow rate, $\dot{m}_f$:

$$\dot{m}_f = \frac{\dot{m}_t}{OF + 1}$$

(3.2)

Oxidiser mass flow rate, $\dot{m}_{ox}$:

$$\dot{m}_{ox} = \dot{m}_f * OF$$

(3.3)

Oxidiser mass, m_{ox}, calculated assuming a burn time, b_t, of 5 seconds:

$$m_{ox} = \dot{m}_{ox} * b_t$$

(3.4)

Fuel mass, m_f:

$$m_f = \dot{m}_f * b_t$$

(3.5)

Volume of fuel, V_f, assuming a ρ_f of 900 kg/m^3:

$$V_f = \frac{m_f}{\rho_f}$$

(3.6)

Wetted fuel surface area, A_{wf}, where $\dot{r}$ is the regression rate with a value of 3 mm/s:

$$A_{wf} = \frac{\dot{m}_f}{\rho_f * \dot{r}}$$

(3.7)

From empirical studies, the propellant combination of N_2O and paraffin wax has an n of 0.5, a of 0.155 mm/s and G_{ox} of 500 kg/m²s [36]. This gave a regression rate value of 3.48 mm/s.

The assumed regression rate enabled the initial sizing of the fuel grain by introducing a constraint on its dimensions. The objective was to determine the optimal length and internal diameter of the fuel grain. Four length-to-diameter (L/D) ratios were analysed, having the dimensions presented in Table 3. Higher L/D ratios were not considered, as they would result in an excessively small internal diameter.

The following equation was utilised to determine the length and internal diameter of the fuel grain. This equation is only related to the wetted fuel surface area and not to the volume of fuel. After determining the dimensions, it was ensured that the fuel grain contained an equal or slightly greater volume of fuel than required.

$$L = \frac{A_{wf}}{(D_i * \pi)}$$

(3.8)

Table 3 - Length-to-diameter values.

L/D	3	5	10	15
Length, L [mm]	146,16	188,69	266,91	342,36
Internal Diameter, D_i [mm]	48,72	37,74	26,68	20,8

Given that the combustion chamber has an inner radius of 54 mm, selecting an L/D ratio of 3 was deemed inappropriate, and to avoid an excessively long combustion chamber, an L/D ratio of 15 was also rejected. Both L/D ratios of 5 and 10 were considered reasonable options. However, the one with the smaller internal diameter (L/D = 10) was chosen as it was the only option that provided the required fuel volume.

3.4. Combustion chamber

As mentioned before, the mechanical steel tube was selected since it satisfied all criteria.

Firstly, it was analysed whether the tube could withstand the pressure using Equation 3.9.

The minimum allowed thickness $h_{(t,min)}$ of the tube is:

$$h_{(t,min)} = \frac{f P_c D_i}{4\sigma_{yield}} \tag{3.9}$$

Where f is the safety factor that took a value of 2, P_c is the chamber pressure with a value of 26 bar, D_i is the internal diameter of the combustion chamber with a value of 54 mm, and σ_{yield} is the yield strength of the steel with a value of 300 MPa. The resulting minimum thickness was 0.234 mm, which in turn resulted in a safety coefficient of 13.5.

The pre-combustion chamber and post-combustion chamber were equally sized, opting for an L/D of 0.5, allowing for the vaporisation of the oxidiser. This results in added sections with a length of 27 mm on each side of the combustion chamber. The finished chambers were slightly bigger (~5 mm) due to the unpredictable shrinking of the paraffin during its cooling.

3.5. Injector plate

The objective of the injector plate is to atomise and distribute the nitrous oxide through the combustion chamber, preferably into the fuel grain port. The chosen geometry and number of the orifices, and their distribution in the injector plate, change the flow rate and its distribution into the combustion chamber, pressure drop values and the atomisation [36].

In a single-phase flow analysis, the fluid is considered incompressible, resulting in a constant mass flow rate, thus allowing for Bernoulli's equation to be applied. Through derivations from the Bernoulli equation and with the addition of a discharge coefficient, C_d, a mass flow rate equation can be expressed by Equation 3.10 [36].

$$\dot{m}_{SPI} = C_d A_2 N \sqrt{2\rho\Delta P}$$

(3.10)

Where C_d is dimensionless and used to account for frictional losses and head losses. Typically ranging from 0.6 to 0.9 in this type of orifice. An assumed value of 0.65 was used for dimensioning. A_2 represents the area of a single orifice, and N represents the number of orifices. ΔP is the pressure differential across the injector and ρ is the density of the injected liquid [36].

For simplification purposes, all orifices have the same diameter. By isolating the area of each orifice in Equation 3.10, the option of adding 10 more orifices, making it twenty-one orifices, was studied, and its values are shown in Table 4. This represented orifices with a diameter of 1 mm, which would be hard to accomplish with perfection. Instead, the option of using eleven orifices was adopted, representing diameters of 1.5 mm.

Table 4 - Calculations to determine the diameter of the orifices.

$\dot{m}_{ox}$ $[kg/s]$	C_d	N	ρ_{ox} $\left[\frac{kg}{m^3}\right], at\ 0ºC$	ΔP	A_2 $[mm^2]$	d_2 $[mm]$	A_{total} $[mm^2]$
0.423	0.650	11	930	700000	1,639	1,445	18,035
0.423	0.650	21	930	700000	0,859	1,046	18,035

However nitrous oxide's high vapor pressure and its compressibility can lead to errors when assuming single-phase and incompressible flow. These errors come from the existence of two-phase flow which significantly alters the flow characteristics. Multiple models have been developed to model two-phase flow, however, coefficients describing various fluid properties are necessary. These properties are not well documented since N_2O is a relatively uncommon commercial oxidiser [36].

From the values given by the calculations performed in Excel, the required oxidiser mass flow rate is 0.423 kg/s. From the available literature, a similar injector design with close to the same oxidiser mass flow rate was found and used as a starting point.

This injector accommodated a showerhead design, eleven orifices with a diameter of 1.4 mm, which are separated equally into two different radii and one in the centre to allow a better distribution of the oxidiser into the chamber. A similar injector provided around 0.400 kg/s of oxidiser flow rate of liquid nitrous oxide with a test bench tank pressure of 60 bar [37].

Considering the fuel grain port's diameter is 26.68 mm, the outermost circumference for the injector holes was chosen to be 22 mm, with the goal of injecting the oxidiser directly into the fuel grain port, and the inner circumference was chosen to be 16 mm for a more homogenous distribution.

Chapter 4 – Case study

4.1. Fabrication processes

To start, a steel cylinder, with a diameter of 90 mm, was cut into the necessary thicknesses using a milling machine. After this, a lathe machine was used to give the components the desired geometry. Some required some extra processes that will be mentioned below.

4.1.1 Fabrication of the injector plate fixation pieces

Starting with the injector fixation component one (IF1), this component had the function of coupling the injection system with the motor, a perforation to allow the screwing of the tubing from the oxidiser tank was made, it can be seen in the right side of Figure 7. It also had the job of spreading the injected oxidiser into the injector plate, allowing for a more homogenous distribution. All the dimensions were given through a lathe machine except the five holes, which were drilled by hand. The geometry of IF1 can be seen in Figure 8.

Figure 7 - IF1 isometric and bottom view.

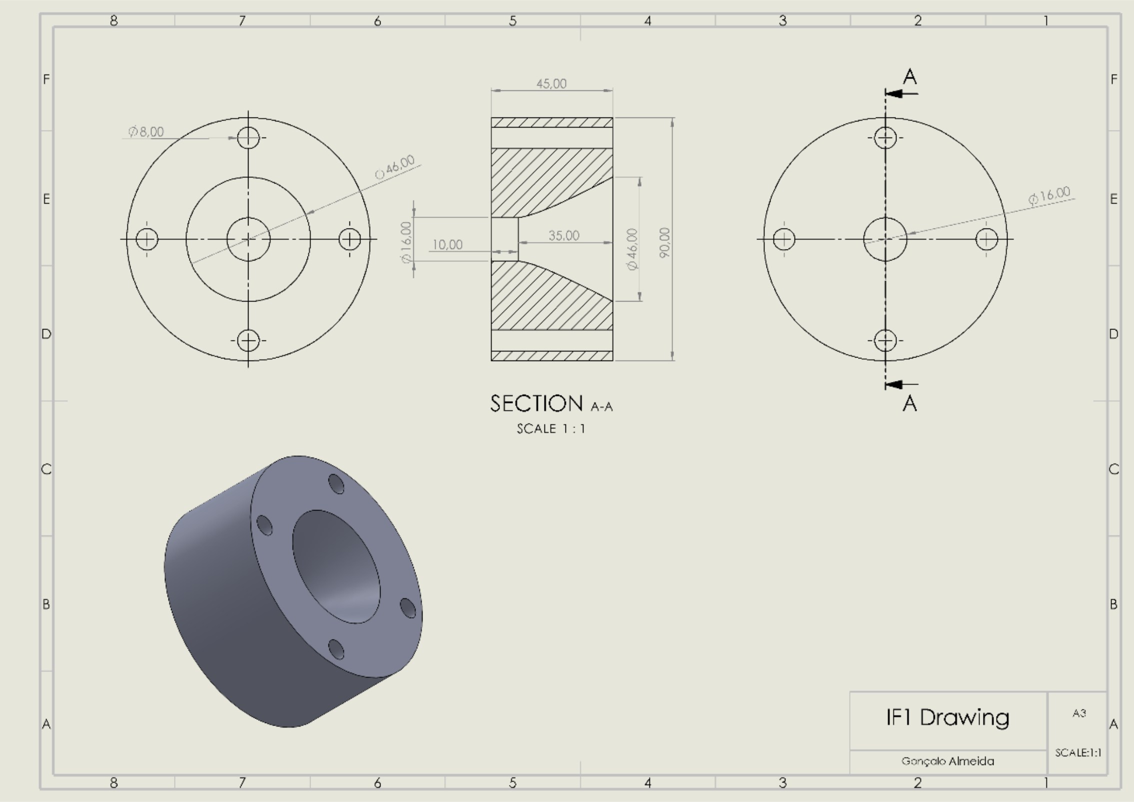

Figure 8 - IF1 technical drawing.

Now relating to the injection fixation component two (IF2), this component had the function of making sure the injector plate was unable to move and seal the combustion chamber on the injection side of the motor. On the left of Figure 9, it's the slight cavity meant to accommodate, with small tolerances, the injector plate. This area of support for the injector plate had to be small, 4 mm, so it allowed the bigger radius of injector holes to be open without compromising the holes made for the threaded rods responsible for making sure the engine's components did not move during its operation. On the right, it's the bigger cavity meant for the accommodation of the combustion chamber. The geometry of IF2 can be seen in Figure 10.

Figure 9 - IF2 isometric views.

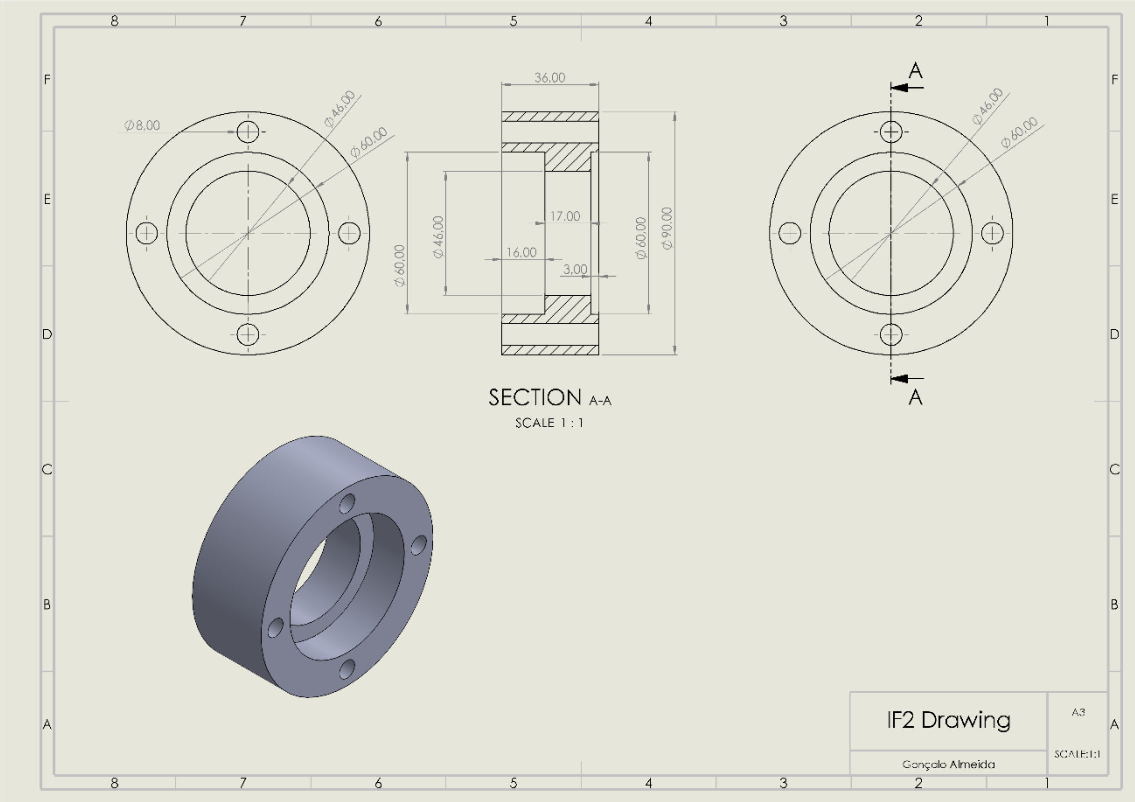

Figure 10 - IF2 technical drawing.

4.1.2 Fabrication of the nozzle fixation pieces

Relating to the components at the end of the motor, components that accommodate the nozzle. Starting with the nozzle fixation component one (NF1). This had the function, just like IF2, to seal the combustion chamber and accommodate the nozzle, and again, just like in IF2, the cavity where the nozzle is has small tolerances to impede the movement of the nozzle during operation of the motor. The perforation in the centre had a diameter slightly bigger (~1 mm) than the intake diameter of the nozzle.

On the right side of Figure 11 is the cavity where the nozzle goes, and on the left side, with the same geometry as in IF2, the cavity for the combustion chamber. The geometry of NF1 can be seen in Figure 12.

Figure 11 - NF1 top and bottom view.

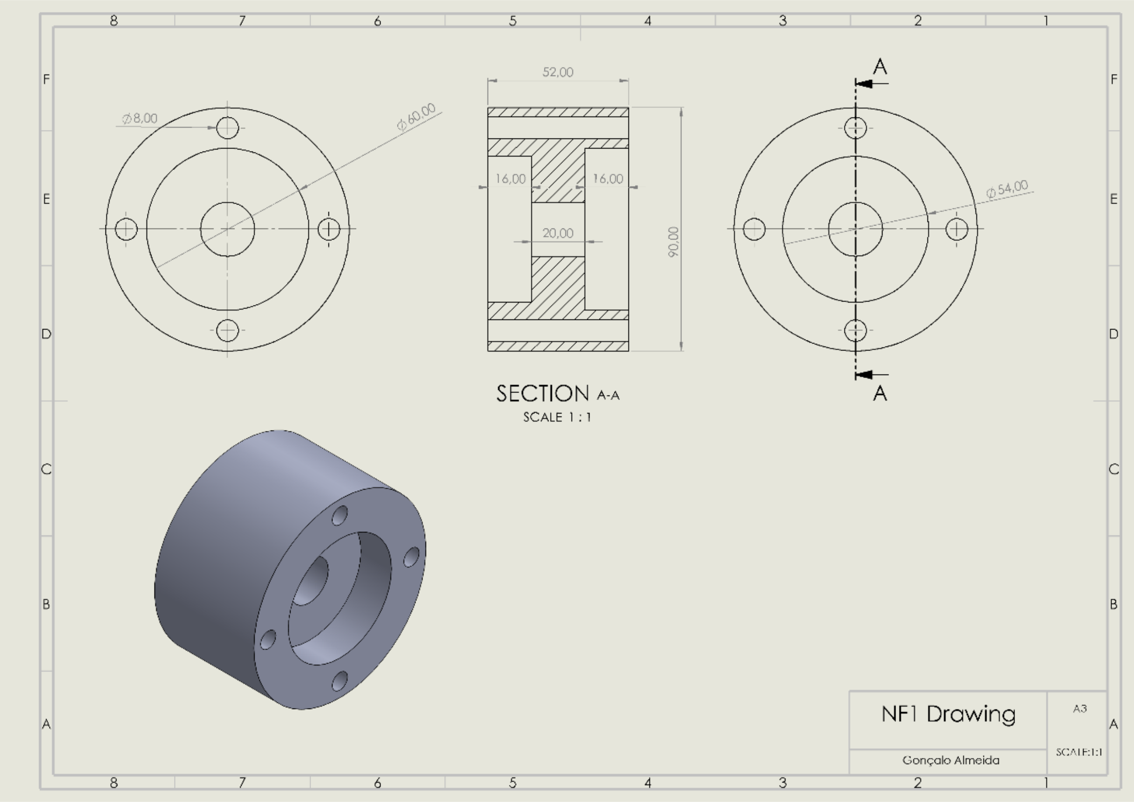

Figure 12 - NF1 technical drawing.

Now, the component at the end of the motor, nozzle fixation component two (NF2), shown in Figure 13, this component had the sole purpose of sealing the nozzle. The diameter of the hole was once again made with small tolerances to avoid the jiggling of the nozzle during operation of the motor. The diameter closely matched the external diameter of the nozzle. The geometry of NF2 can be seen in Figure 14.

Figure 13 - NF2 isometric and top view.

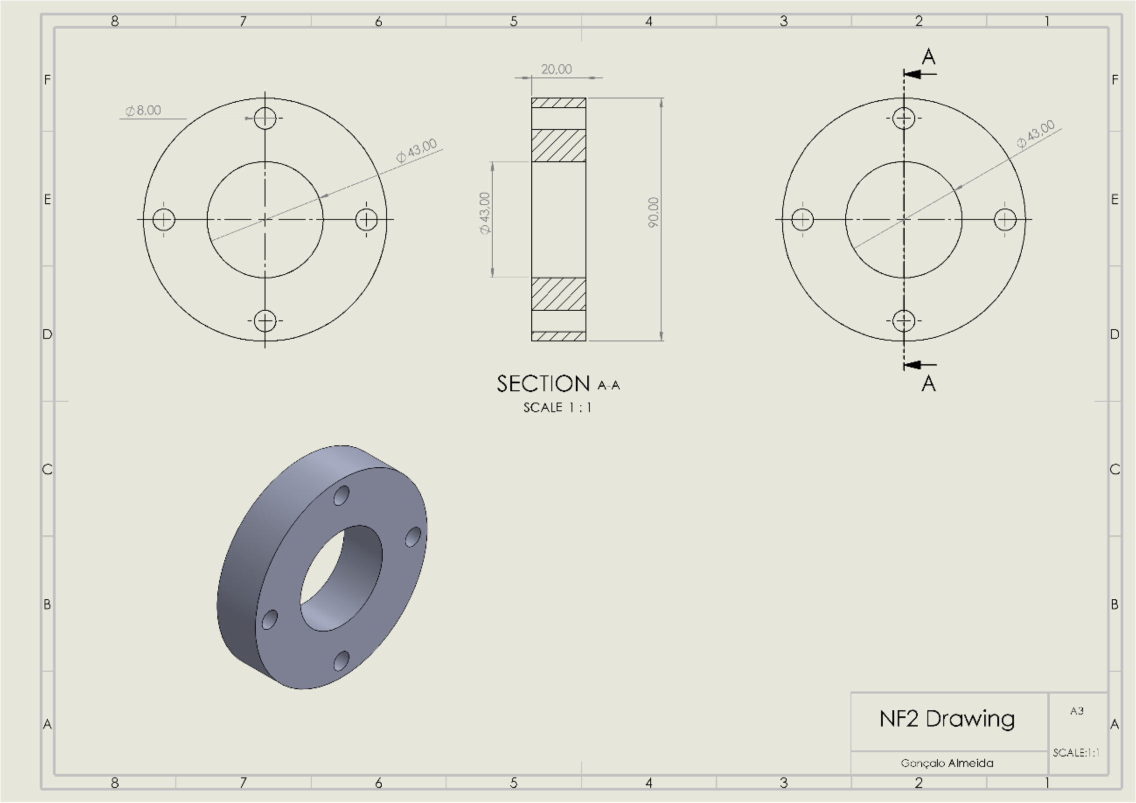

Figure 14 - NF2 technical drawing.

4.1.3 Fabrication of the injector plate

Now comes one of the most critical components of the motor, the injector plate. Shown in Figure 15 and represented in Figure 16, this component had its dimensions, especially its diameter, constrained by the previously talked IF1 and IF2 components; the diameter was maximised for better structural integrity, not allowing bigger diameters because of the reason given before in the IF2 section. This component was fabricated with the lathe machine and the holes were made by hand with a drill. The location of the perforations was previously marked with the help of a pen and paper. The desired location of the perforations was drawn on a piece of paper and then transposed into the injector plate with the help of a pricker.

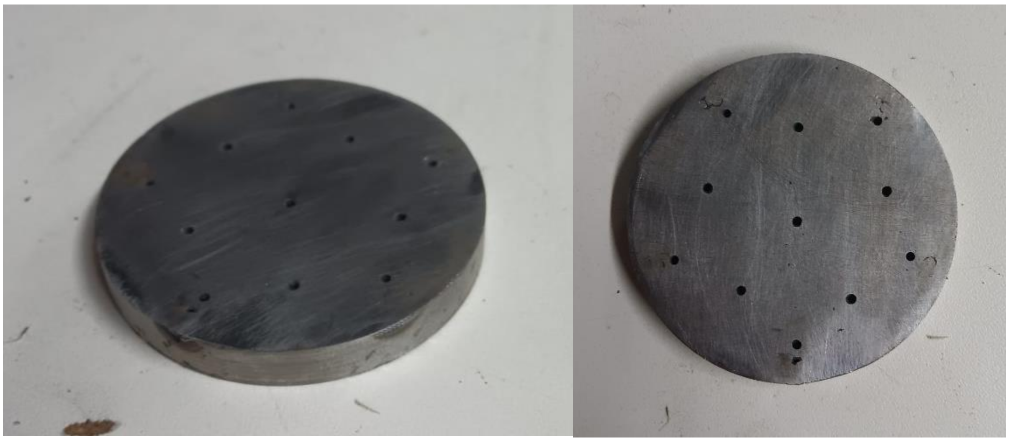

Figure 15 - Injector plate isometric and top view.

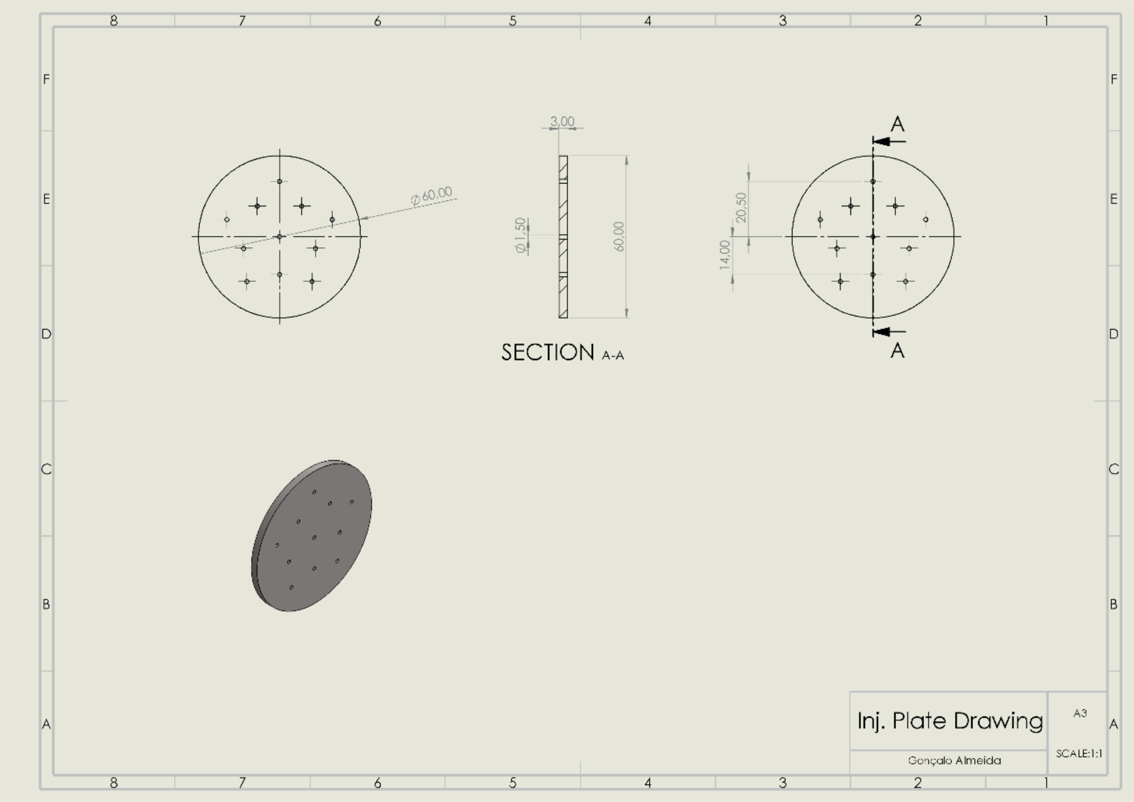

Figure 16 - Injector plate technical drawing.

4.2. Hardening process

Hardening of the fixation pieces and, most importantly, the injector plate showed to be a necessity, a quick study utilising the SolidWorks software proved that the steel being used to fabricate these components was insufficiently hard, resulting in bending in the injector plate. To use this steel instead of acquiring a new one, a hardening process was proposed. Two similar processes were used due to the appearance of small imperfections in the components in the first process. The first process consisted of heating the components in an oven to 1020°C, followed by quick cooling using oil. This process was unsuccessful since after the second component entered the bucket filled with oil, which had already been heated by the previous component, it started a small fire. This was justified due to the presence of impurities in the oil. To prevent this, a second method was proposed, instead of using oil as a coolant, salinised water was used. Two kilograms of salt were poured into 20 litres of tap water. This method proved to be safer.

Values corresponding to the hardness before and after the processes are presented in Table 5. Three tests were performed in the final components, the averaged values are the ones represented in Table 5.

Table 5 - Initial and final hardness values with the different cooling methods.

Component	Initial HV	Final HV (Average)	Cooling method
Injector plate	214	541	Oil
IF1	214	541	Oil
IF2	214	345	Salinised water
NF1	214	345	Salinised water
NF2	214	345	Salinised water

After the hardening process, cleaning was required due to the accumulation of rust over time. The cleaning process consisted of the utilisation of an ultrasonic cleaner machine and scraping the excess. Figures 17 to 20 show the components in their final state.

Figure 17 - IF1 after hardening and cleaning processes.

Figure 18 - IF2 after hardening and cleaning processes.

Figure 19 - NF1 after hardening and cleaning processes.

Figure 20 - NF2 after hardening and cleaning processes.

4.3. Fuel grain fabrication

The mass of paraffin wax needed for the fuel grain dimensions was weighed and melted at 100 °C in a pan using an electric heater. After a few minutes, the completely molten paraffin wax was poured into the preheated combustion chamber. To achieve the required port in the middle, a tube with a plate soldered to the bottom was placed inside the combustion chamber tube, shown in Figure 21. The molten wax was then left to cool at room temperature. The combustion chamber tube was sealed at the bottom using a 3D printed piece, made of ASA with the purpose of not letting wax flow into the pre-combustion chamber or post-combustion chamber area, as they are equally sized. This piece, represented in Figure 22, had a diameter of 54 mm, matching the inside of the combustion chamber, and a height of 27 mm, the desired length of the pre-combustion chamber and post-combustion chamber. Figure 23 is the finished fuel grain inside the combustion chamber.

Figure 21 – Component used to create the fuel grain port.

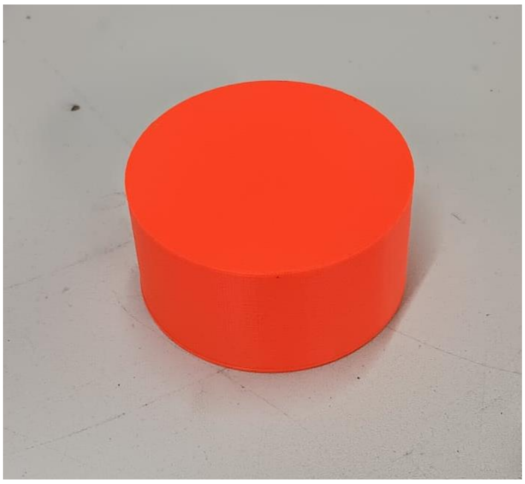

Figure 22 - 3D printed ASA piece.

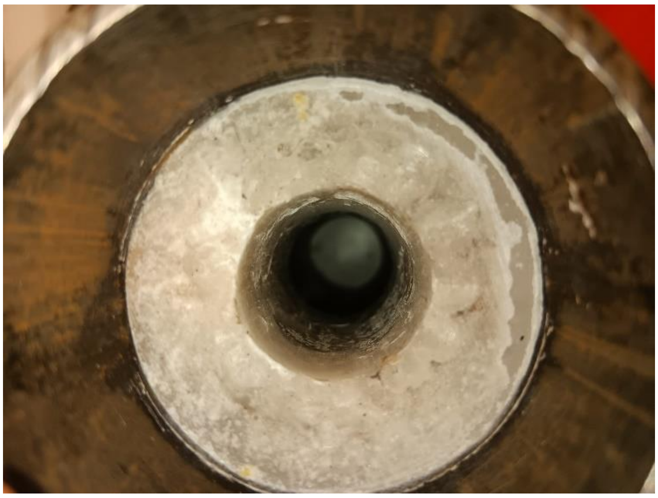

Figure 23 - Solidified fuel grain inside the combustion chamber.

4.4. Ignition charge fabrication

The ignition charges were initially intended to only be comprised of a gunpowder ball sealed with a plastic with a nichrome wire going through the ball. This proved to be an insufficient heat source. To allow a more direct contact with the heat source a “cookie” like mould was made, the goal was to make a mixture of paraffin and gunpowder, this would allow the paraffin to be in direct contact with the gunpowder and after receiving heat instantly liquify all the paraffin in the cookie (see Figure 24, 25 and 26). After experimenting with different amounts of each component, the finished cookies had approximately 10 grams of paraffin and 6 grams of gunpowder.

Figure 24 - Charge mould with nichrome wires.

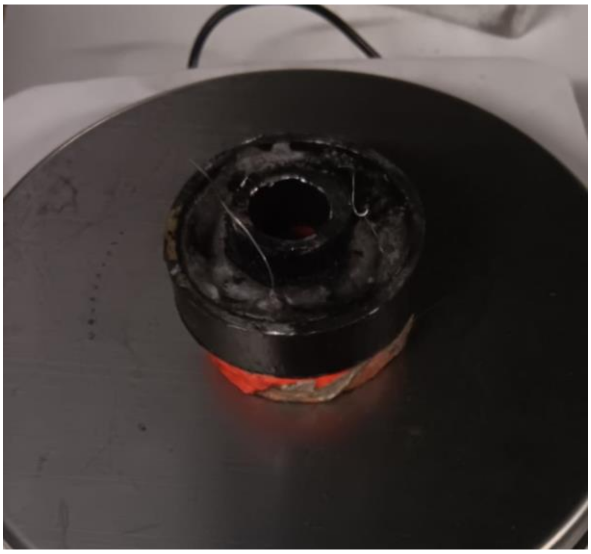

Figure 25 - Finished charge inside the mould.

Figure 26 - Charge inside the motor.

4.5. Experimental apparatus

In this section, all the experimental apparatus will be shown and explained.

4.5.1 Motor sealing

To ensure the motor remains sealed during operation, the following calculations were made: [38]

Beginning with the calculation of the pressurised area, with r being 0,027 m, half of the internal diameter of the combustion chamber.

$$A = \pi * r^2$$
$$A = 0{,}00229\ m^2$$

This in turn results in a force of (assuming 26 bar of pressure):

$$F = P * A$$
$$F = (2{,}6 * 10^6) * 0{,}00229$$
$$F = 5954{,}57472\ N$$

With a bolt from the SAE Class 8.8, the bolt stressed area (A_t) is 99,65 mm^2 and the proof strength (σ_{proof}) is 600 MPa.

$$F_{\max per\ bolt} = A_t * \sigma_{proof}$$
$$F_{\max per\ bolt} = (99{,}65 * 10^{-6}) * (600 * 10^6)$$
$$F_{\max per\ bolt} = 59790\ N$$

Since there are 8 bolts:

$$F_{\max total} = 59790 * 8$$
$$F_{\max total} = 478320\ N$$

Comparing the required force to resist the pressure with the available holding force:

$$F_{\max total} = 478320\ N \gg 5954{,}6\ N = F$$

Resulting in a safety factor of:

$$SF = \frac{F \max total}{F}$$

$$SF = \frac{478320}{5954{,}6} = 80{,}3$$

4.5.2 Test bench

A vertical configuration was chosen for the motor during operation, which provides more stability, safety and reduced drag between the motor and the support beams. Ideally, the applied force is in the soil's direction, hence, no forces would be applied in the support beams. To build this bench, a base that was available in the university was used; it showed good structural integrity, hence it was concluded that it was a satisfactory choice. The four support beams were purchased; it was opted for “L” shaped beams with 500 mm of height and a 30 mm by 30 mm base. Both the base and the beams were made of steel. These beams were soldered to the base, leaving a gap in the middle to place the rocket motor (Fig. 27). When the motor is in its position on the test bench, it has a gap of around 5 mm to the support beams. A perforation was made in the middle of the base, where the motor will be placed, to allow for the screwing and well tightening of the load cell responsible for measuring the thrust values during operation.

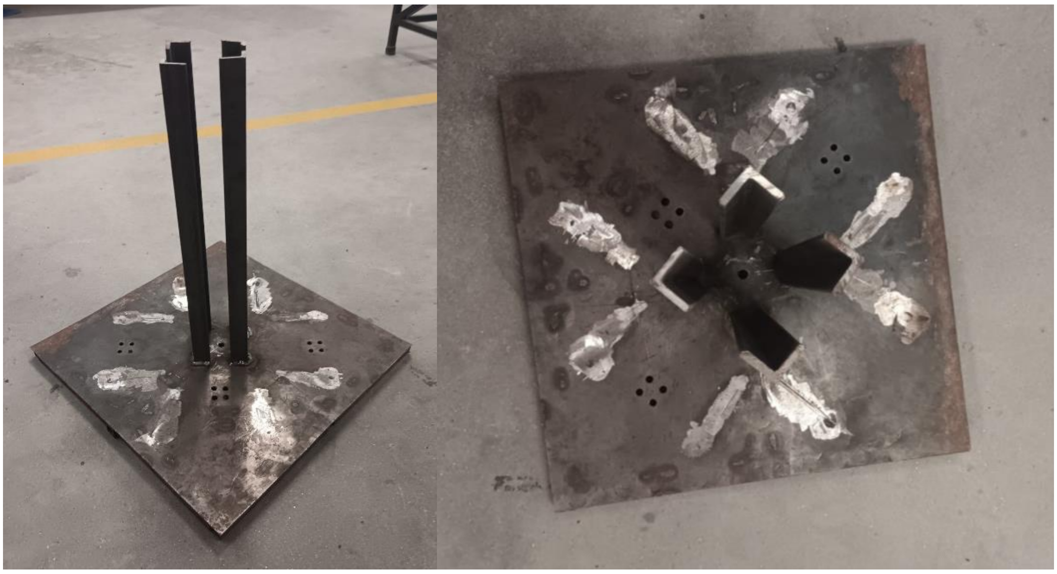

Figure 27 - Test bench's isometric and top views.

4.5.3 Feeding system

The feeding system comprises a nitrous oxide tank, a pressure regulator, a solenoid valve and a stainless-steel pipe. The pressure that comes out of the tank was regulated by the pressure regulator that was incorporated right out of the tank's cap, as shown in Figures 28 and 29. This pressure regulator was then coupled right into the solenoid valve, which is responsible for allowing/disallowing the flow. This valve is then mounted to a stainless-steel pipe, which was then connected to the motor (Fig. 30).

Figure 28 - Nitrous oxide tank coupled with a pressure regulator.

Figure 29 - Pressure regulator.

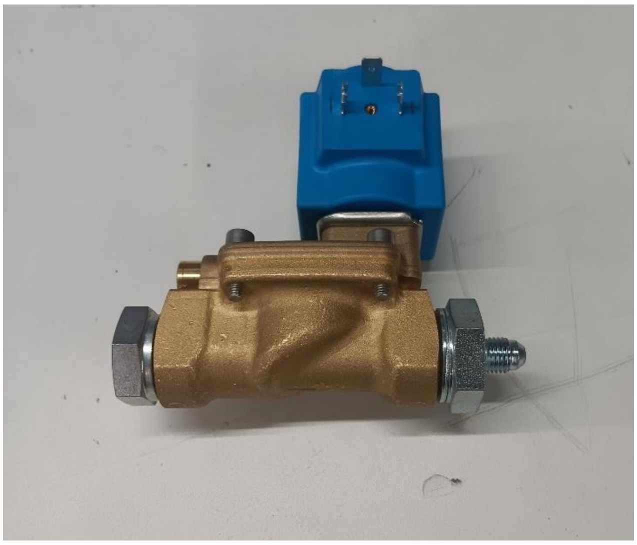

Figure 30 - Solenoid valve.

4.5.4 Control and data acquisition systems

The control and data acquisition system is comprised of two subsystems. The ignition control system (ICS) and the data acquisition system (DAS). The ICS uses an Arduino Uno incorporated with an ATmega328P microprocessor, while the DAS uses an Arduino Mega 2560 with an ATmega2560 microprocessor. Both systems utilised the same LoRa radio module for communication between them. ICS's function is, as the name suggests, to control the ignition; it sends an ignition message to DAS, starting all its subsystems. For redundancy purposes, ICS also receives the data from DAS, this data comes in larger time gaps than the recorded one in DAS. DAS's function is to initiate ignition, injection, read and convert the data from the sensors and save it in an SD card.

4.5.4.1 Power supply

Both systems have different power supplies; ICS is powered by a computer through a USB port, while DAS is powered by a 12V battery. Both power supplies were almost forced since a computer was required for the ignition message to be sent via Arduino IDE's serial monitor, and batteries, since the tests would be made in an area where electricity was not available.

4.5.4.2 Radio module

For the communication between the ICS and the DAS, LoRa technology was chosen due to its low power consumption and long range, allowing for safe testing. The "Grove-LoRa radio 433MHz", developed by "Seeed Studio", was selected. It has an RFM98 module based on the Semtech SX1276 LoRa®, the processor for the module is an ATMEGA168.

This module has three programmable parameters: the bandwidth, the spreading factor and the coding rate. Since the standard parameters initially worked, they were not altered; these parameters are: bandwidth 125 kHz, spreading factor 7 and coding rate 4/5.

4.5.4.3. Ignition system

The ignition system is simple, comprised of a battery with the negative terminal connected to a nichrome wire, which is then connected to the COM port on the relay, and the positive terminal directly connected to the NO (Normally Open) port. This connection changes state once the ignition message is received by the Arduino and sent to the relay through the change in state of a digital pin. Once the relay activates, the battery is now connected to the ignitor, comprised of the nichrome wire and a mixture of paraffin and gunpowder.

4.5.4.4 Sensors

In this system, three sensors were implemented: two load cells, one responsible for measuring the motor's thrust and the other the nitrous oxide tank weight, and a pressure sensor to measure the pressure inside the combustion chamber.

4.5.4.4.1 Load cells

Considering the maximum expected traction values, a 200 kg type "S" load cell was chosen (Fig. 31). For the tank weight reading a 30 kg load cell was enough hence chosen (Fig. 32). These sensors use a "wheatstone bridge" structure which measures the applied force through variations in its internal resistance. This change in resistance is due to the suffered extensions when tension is applied.

Since the output voltage of the load cell is too low, it is required to alter this analogic signal for possible interpretation by the ATmega2560, this is HX711's task. The HX711 is an amplifier and an analogic to digital converter, which conditions the signal for a possible interpretation, without noise. This module is directly connected to ATmega2560 through four pins: GND, VCC, Data (DT), and Clock (SCK).

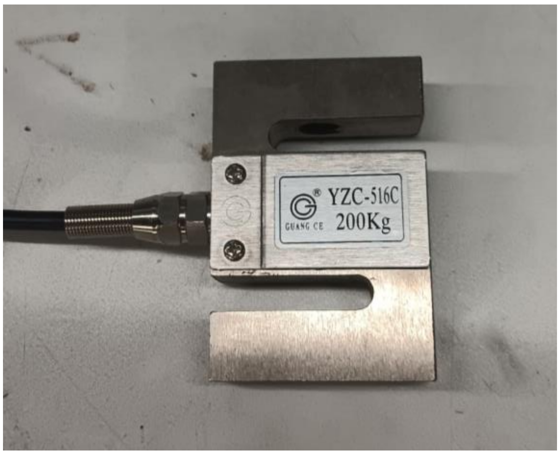

Figure 31 - Load cell used for traction readings.

Figure 32 - Load cell used for tank weight readings.

4.5.4.4.2 Pressure sensor

The used pressure sensor (Fig. 33) has an output signal between 0,5 V and 4,5 V, allowing for a direct interpretation from ATmega2560. The range of the sensor is comprised from 0 to 500 psi (~34,47 bar). Considering that this sensor was not developed to make readings from combustion gases, a hydraulic tube filled with hydraulic fluid was equipped from the engine to the sensor. The output voltage of the sensor is a linear function of the detected pressure, which is represented by Equation 4.1.

$$p = \frac{500 - 0}{4{,}5 - 0{,}5} * (V_{out} - 0{,}5) \tag{4.1}$$

For ATmega2560 to be able to interpret the output voltage, this one is converted into integer values ranging from 0 to 1023, where 0 corresponds to 0 V and 1023 corresponds to the voltage that feeds ATmega2560 itself (5 V). The “sensorValue” is the result of the conversion from voltage to an integer value and is represented by Equation 4.2.

$$V_{out} = \frac{5}{1023} * sensorValue \tag{4.2}$$

Figure 33 - Pressure sensor.

4.6. Implementation

The ICS and DAS circuits will be shown and explained (Fig. 36, 37 and 38), as well as the PCB utilised with the DAS. The PCB shown in Figures 34 and 35 was used since it allowed for the necessary connections.

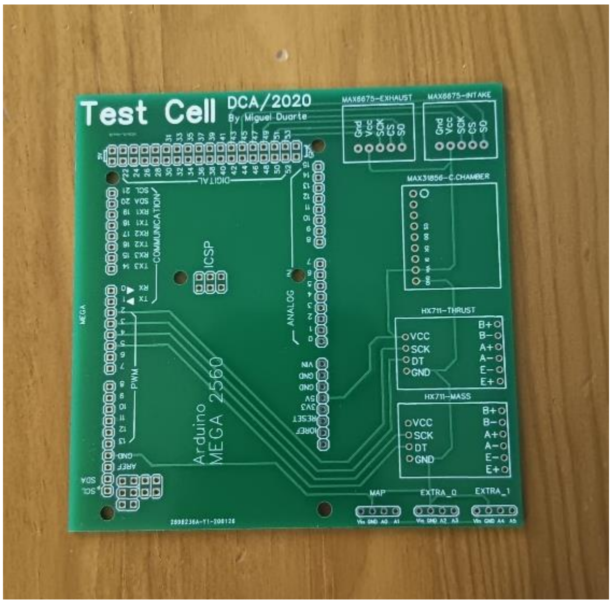

Figure 34 - PCB used in the DAS.

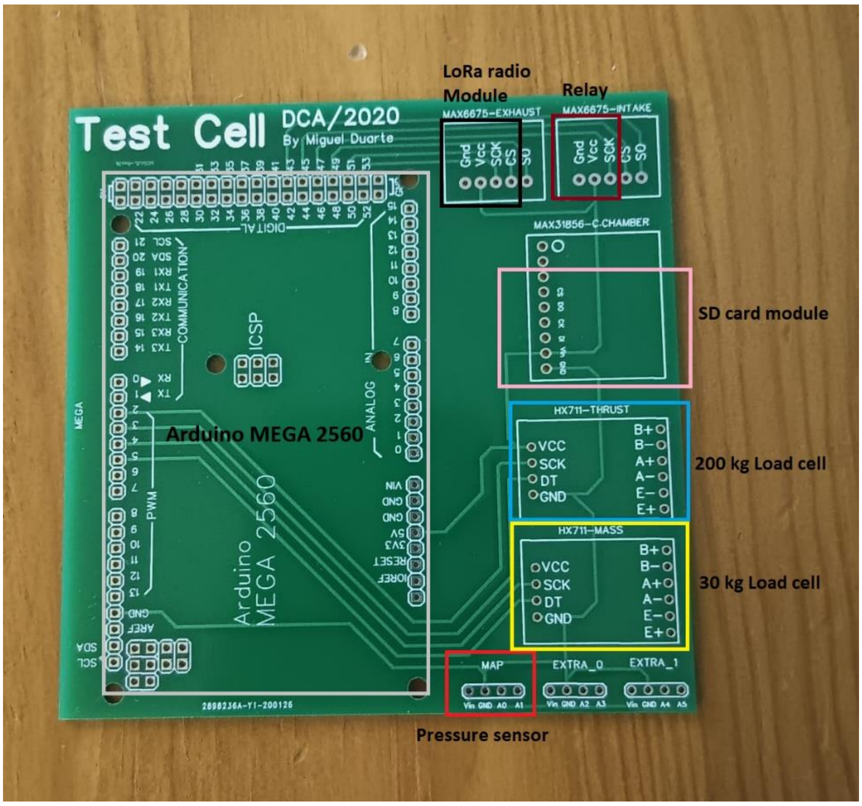

Figure 35 - PCB with a representation of the connections.

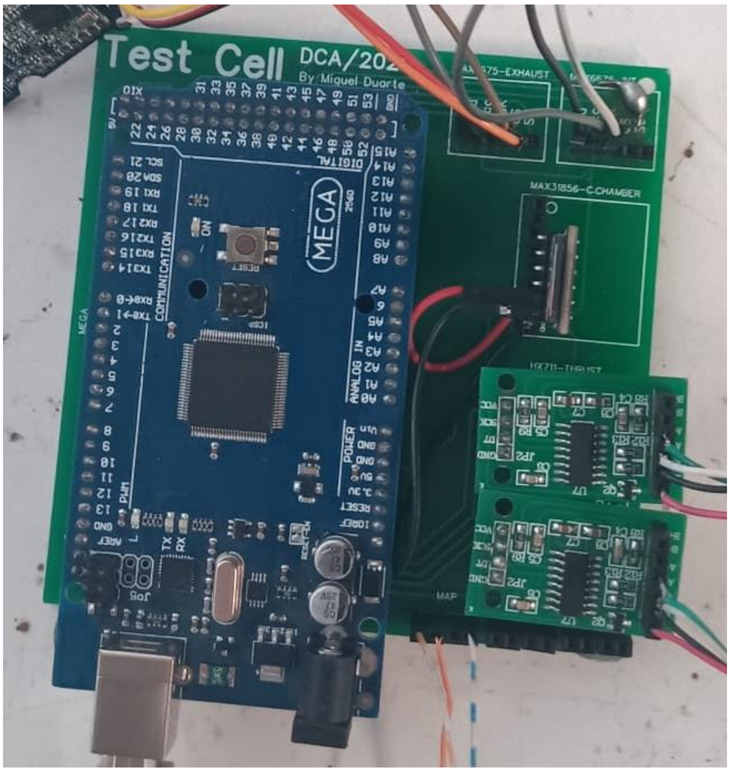

Figure 36 - DAS.

It is worth noting that a slight alteration was required in the SD card module connections since it needed a 3.3 V power source, but there were no 3.3 V pins left. A similar adaptation was made since a GND (ground pin) was unreachable. This extra wiring is shown in Figure 37. Referring to Figure 37, in the left figure, the red wire connects the MISO pin from the SD card to a digital pin (D39), and the black wire connects the GND pin. On the figure to the right, the connection made allows for the SD card to be powered by a 3.3 V pin.

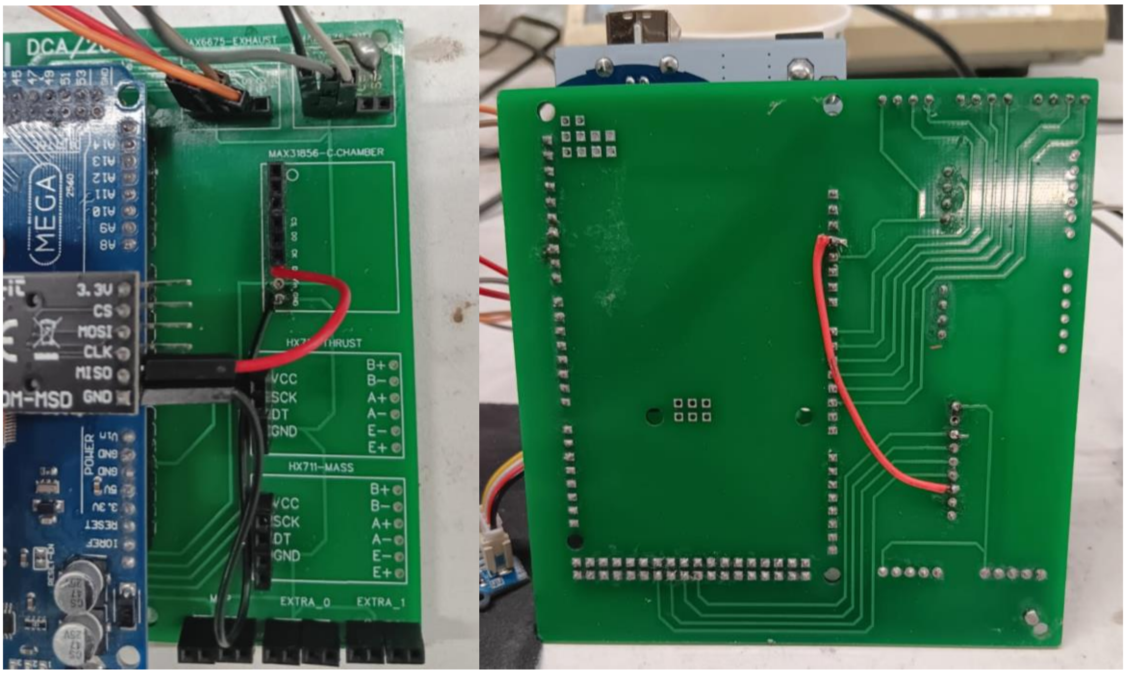

Figure 37 - Extra necessary wiring on the PCB.

The implementation of the ICS was much simpler since it only required the LoRa module to send the ignition message to start the DAS. ICS is represented in Figure 38.

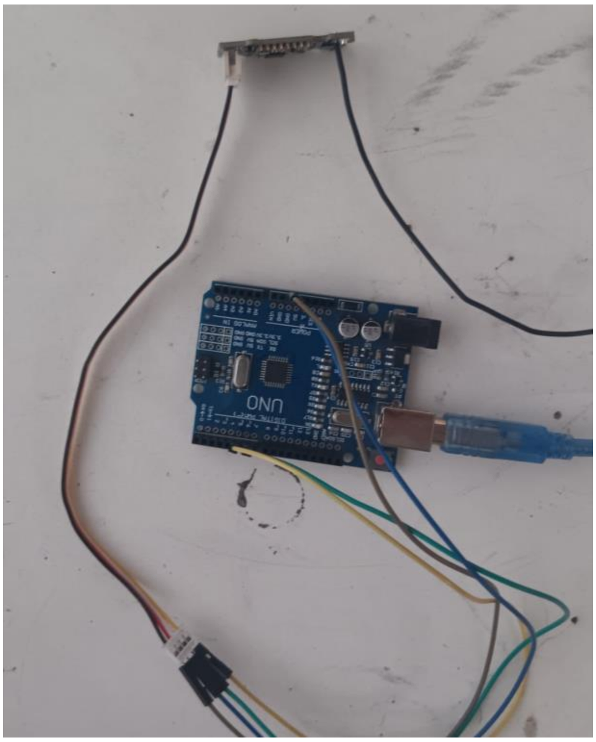

Figure 38 - ICS.

4.7. Preliminary tests

The main goal of the preliminary tests was to determine the real oxidiser mass flow rate and to ensure the structural integrity of the injector plate during the injection process. The real oxidiser mass flow rate was not successfully determined due to the small amount of nitrous oxide available, avoiding waste; the injection time was very small (~1 second), reaching around 60 bar of injection pressure, ensuring the structural integrity of the injector plate during the injection process.

Multiple tests were conducted with the paraffin/gunpowder charges. Initially it was tested the use of gunpowder sealed with some plastic was tested; this idea was dismissed since it was clear that the gunpowder was not releasing enough heat to liquify the paraffin near the injection plate. After, there was the idea to create a “cookie” like comprised of paraffin mixed with gunpowder. This showed potential since, after quite some testing with the amounts used in the cookie, there was liquidation of the paraffin (initially only some of the paraffin liquified and the gunpowder was not exploding, the paraffin was absorbing all the heat from the nichrome wire, this was due to a non-ideal amount of each substance, bigger amounts of gunpowder removed this scenario). With some improvement in the manufacturing process of the cookie and the addition of one more nichrome wire to allow a more uniform heating of the cookie, the idea proved to be a success.

Chapter 5 – Discussion of results

In this chapter, the results from the hot fire tests will be presented and discussed.

Hot fire test 1:

This hot fire test was unsuccessful. From the analysis of the grain and the paraffin/gunpowder charge after the test, it was presumed either a lack of heat from the charge and/or excessive injection pressure, resulting in the extinction of the existing flame. It was also noted that the paraffin grain showed close to no change in its geometry, further showing the lack of heat inside the combustion chamber.

Hot fire test 2:

Considering what was learnt from the previous test, in the second attempt, the injection pressure was lowered to 30 bar from 40 bar. There was also the addition of an extra ~10 grams of gunpowder directly from the nozzle. These alterations proved to work better, resulting in a successful test (see Figures 39 and 40), even though the results were not close to the theoretical predictions.

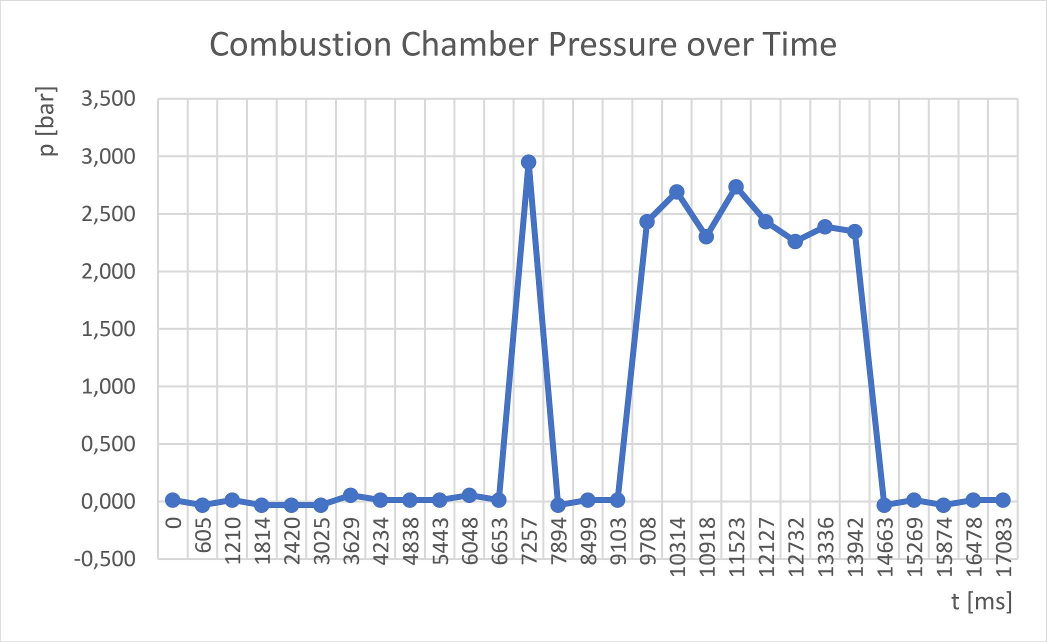

Figure 39 - Combustion chamber pressure over time.

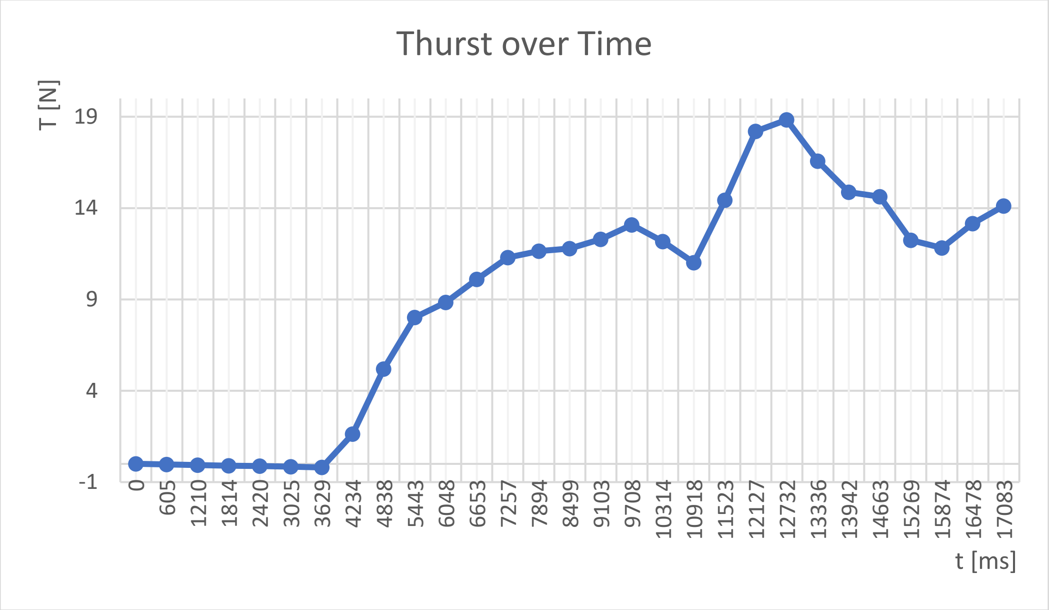

Figure 40 - Thrust over time.

Analysing the previous graphs, beginning with Figure 39, it is visible where the initial injection of 0.5 seconds was made, around 7257 ms, resulting in a spike of pressure, after this spike there is the 5 second injection, from 9708 ms to 13942 ms where the pressure remained modest but close to constant.

From Figure 40, where the thrust values are shown it is visible a steady increase in thrust from 3629 ms to 9708 ms, this increase begins right after the ignition message was sent (sent at 3025 ms), the small delay is a consequence of the paraffin/gunpowder charge requiring some time to first liquify the paraffin and then heat the gunpowder resulting in its explosion.

Now referring to the 5 second injection time, it is noticeable a slight drop in thrust right after the injection begins (10918 ms), something that should not occur, this can be explained with the assumption that the load cell and motor were not properly coupled, resulting in the moving and not proper alignment with the load cell, this can be further supported by analysing the thrust values after the injection ends, there should be a rapid drop in thrust but there was a slight increase some seconds after.

5.2 The injection system problem

There is a clear problem with the injection system design, the system did not provide nearly enough nitrous oxide as intended. Here are some of the reasons why this occurred and how to fix it for the future.

The oxidiser feed system exhibited lower than expected performance, with a measured average nitrous oxide flow rate of approximately 57 g/s, substantially below the intended 423 g/s value for optimal performance. While the injector plate design was inspired by successful implementations in literature, featuring 11 orifices of 1.5 mm diameter each, significant flow restrictions were observed in practice. A key factor contributing to this discrepancy was likely partial vaporisation of the nitrous oxide before injection. The system included a pressure regulator set to 30 bar, which corresponds to a boiling point of around 18.3 °C for N_2O. It is believed that heating of metallic components of the feed system, particularly the injector cone and feed line, caused local temperatures to exceed this threshold while the system sat idle before ignition. Despite the relatively short exposure time, brief contact with these warmed components was likely sufficient to trigger localised vaporisation, especially near the injector orifices where pressure drops and turbulent mixing occur. This scenario is supported by visual observations of white, bubble-like formations at the injector entrance, as shown in Figure 41, characteristic of two-phase flow conditions. Such partial flashing results in reduced liquid flow, increased pressure losses, and potential flow choking, all of which can drastically reduce the amount of oxidiser mass delivered to the combustion chamber. This ultimately led to a lower O/F ratio, contributing to the modest regression rate observed and underperformance compared to theoretical predictions. In future designs, thermal insulation of the feed lines and injector block and minimising idle time should be considered strategies to prevent premature vaporisation and ensure reliable oxidiser delivery.

Several factors in the oxidiser feed system design likely contributed to the insufficient mass flow rate observed during testing, and future designs should address these through improved injector and feed system optimisation. Injector sizing and area optimisation are critical to achieving the desired oxidiser mass flux. In this test, the total injector area may have been too small relative to the pressure drop available, which limited the achievable flow rate. Enlarging the injector holes or increasing their number, while maintaining appropriate discharge coefficients, could enable higher oxidiser flow. Also worth mentioning that increasing chamber pressure by diminishing throat diameter would reduce the pressure differential required for the target oxidiser flow, by minimising the pressure difference across the injector, the flow remains more stable and is more likely to stay in the liquid phase. Additionally, avoiding sharp bends or excessive lengths in the feed line is essential, in the current system the feed line was ~2 meters but it did have a bend near the pressure regulator as seen in Figure 42, these features introduce pressure losses and create regions of turbulence where nitrous oxide is prone to flashing into vapor, especially near warm surfaces. The orientation of the oxidiser tank and the strategy used for liquid draw are also very important. Drawing from a tank upright and near the ullage, as was done in this test, increases the likelihood of injecting vapour-phase N_2O. Inverting the tank to ensure consistent withdrawal from the liquid phase would significantly enhance oxidiser delivery. These improvements would lead to more reliable engine operation and a more accurate representation of hybrid combustion behaviour.

Figure 41 - IF1 after testing shows white bubble-like formations.

Figure 42 - Nitrous oxide tank with a bend in the feed line.

5.3 Time-averaged regression rate

The regression rate was calculated as follows:

1. The volumetric change in the fuel grain was calculated using a measuring cylinder. The results are shown in Table 6.
2. The burn time was 5 seconds, so a time-averaged regression rate was calculable.

Table 6 - Fuel grain volume difference.

Volume (cm^3)	Test 2
Initial	398,01
Final	259,03
Difference	138,98

Since the burn time (t_b) was predetermined to be exactly 5 seconds, it is now possible to calculate the average regression rate using Equation 5.1.

$$\dot{r}_{avg} = \frac{R_f - R_0}{t_b} = \frac{18{,}5 - 13{,}5}{5} = 1\ mm/s$$

(5.1)

It is worth mentioning that the measurement of the final radius (R_f) has a margin of error since the measuring cylinder can only measure the innermost part of the grain. A ±1 mm measurement error in final port diameter results in a ±0.2 mm/s alteration in regression rate.

The regression rates calculated above can't be compared to other available research, since a lot of factors influence the regression rate, such as the oxidiser mass flux, oxidiser choice, fuel composition, length of the carbon chain and type of motor.

The average regression rate measured during the test was approximately 1.0 mm/s, which falls within the lower end of values reported for paraffin-based hybrid rocket engines using nitrous oxide as the oxidiser. This result aligns with observations by Liu et al. in *Regression rate of paraffin-based fuels in hybrid rocket motor*, where the regression rate was shown to depend on factors such as oxidiser choice, very slightly on chamber pressure, and injector design. In the present case, the observed uniformity in fuel consumption along the grain length and the presence of wave-like structures on the inner port surface are characteristic of liquefying paraffin fuels, supporting early-stage entrainment behaviour but still being majorly reliant on the regression rate through vaporisation due to the low mass flux values.

Unfortunately, the oxidiser tank mass load cell system appeared to malfunction since it showed no reduction in its weight during both tests. By measuring the tank's weight after the tests, it was possible to retrieve the average consumption of oxidiser, resulting in an average oxidiser flow rate of 57 g/s.

The measured oxidiser mass flow rate of approximately 57 g/s, combined with a calculated fuel consumption of 25,3 g/s, results in an O/F ratio of 2.25, which falls within the expected range for paraffin–nitrous oxide hybrid rocket systems operating without regression-enhancing mechanisms. Literature indicates that such systems typically exhibit O/F ratios between 2 and 4, with corresponding regression rates of 1–3 mm/s under modest chamber pressures and laminar flow conditions [31],[39]. The observed regression rate of approximately 1.0 mm/s is therefore consistent with the reported oxidiser flow and is characteristic of non-optimised configurations lacking swirl injection or turbulent flow induction. This is further supported by experimental observations: the burn progressed smoothly and uniformly along the grain length, the paraffin surface exhibited a wave-like texture typical of liquefying fuels, and no signs of combustion instability or erosive burning were present (Fig. 43).

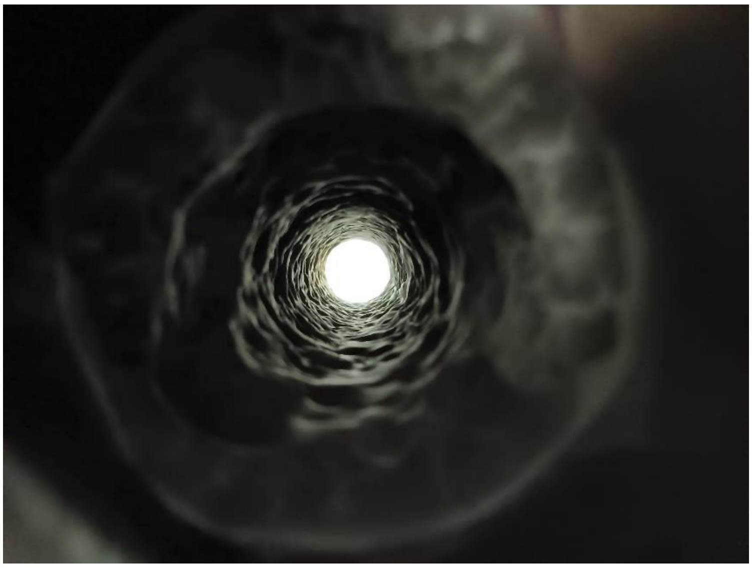

Figure 43 - Paraffin grain port after test 2.

Chapter 6 - Final considerations

6.1. Conclusions

In the initial design phase, an oxidiser-to-fuel O/F ratio of 6.8 was selected based on CEA simulations maximising specific impulse for the paraffin/nitrous oxide combination. However, experimental data and post-burn analysis indicate that this assumption was not aligned with the actual behaviour of the system. The modest chamber pressure (~2 bar), absence of regression-enhancing mechanisms, and the measured regression rate of approximately 1 mm/s suggest that the actual O/F ratio was closer to 2.25, a value more consistent with similar paraffin–nitrous oxide hybrid systems operating under comparable conditions. This highlights the importance of basing early design choices, such as expected oxidiser flow or O/F ratio, on realistic numbers that come from actual performance data or proven design guidelines and not just ideal cases.

With an average regression rate of approximately 1 mm/s and a modest chamber pressure of ~2 bar, the fuel mass flow rate was significantly constrained. As a result, the system was unable to achieve the oxidiser flow rates necessary to sustain such a high O/F. In future designs, the approach should be reversed: begin by estimating how much fuel can realistically be burned based on the grain geometry and a reasonable regression rate from the literature, coupled with expected oxidiser flow rates based on the injector and pressure conditions. These estimates will give a more accurate O/F ratio, which can then be used in thermochemical tools like NASA CEA to predict realistic performance outcomes.

This study explored the regression rate behaviour of paraffin-based fuels in a hybrid rocket motor utilising nitrous oxide as the oxidiser. The experimental tests provided insights into what influences fuel regression in hybrid rocket engines and identified several key areas for further improvement and optimisation.

Key Findings

1. **Regression Rate Behaviour**: The average regression rate measured was approximately 1.0 mm/s, which aligns with values observed in similar paraffin-based hybrid systems operating under moderate pressure conditions. This value is consistent with the low end of expected regression rates for unaugmented systems using paraffin as fuel and nitrous oxide as oxidiser. The consistent fuel consumption along the port length, coupled with the wave-like texture observed on the burned surface, suggests that the system was operating

in a surface melting and vaporisation-driven regression mode, rather than one dominated by droplet entrainment. This possibly occurred due to a lack of oxidiser in the combustion chamber, a lack of pressure during combustion and minimal turbulent flow.

2. **Design Considerations and Additives**: The experimental results show the need for further optimisation in the system design. Specifically, the nozzle design should be revised to include a smaller throat diameter to increase chamber pressure and enhance convective heat transfer. Moreover, the addition of metal particles like aluminium to the paraffin fuel could provide additional energy to the combustion process, increasing the regression rate by promoting secondary combustion and enhancing heat feedback to the fuel surface. Future work should also consider swirl injection or other modifications to the injector geometry to improve flow mixing and enhance overall combustion efficiency.

3. **System Design Optimisation**: Based on the results, the design of future tests should prioritise improving the convective heat transfer to the fuel surface. This can be achieved by increasing chamber pressure within the limits of the kinetically-limited regime where fuel regression is still controlled by surface heat transfer, optimising nozzle and injector geometries, and introducing heat transfer enhancing strategies. Additionally, further exploration of metallic additives or other fuel augmentation techniques could lead to increased regression rates and overall system performance.

Final remarks

This research provides experimental data on the regression behaviour of paraffin-based fuels in hybrid rockets and brings up key challenges and opportunities for future optimisation. By addressing the limitations of the current experimental setup and exploring more advanced system designs, hybrid rocket technology can continue to advance into more efficient and scalable propulsion systems. As the field evolves, further refinement of fuel and oxidiser dynamics, nozzle and injector optimisation, and the integration of advanced combustion diagnostics will play critical roles in realising the full potential of hybrid rocket systems.

6.2. Future works

The results of this experiment offer multiple opportunities for further investigation and development in the paraffin-based hybrid rocket propulsion field. While the test successfully demonstrated consistent fuel regression and provided useful insight into the combustion behaviour of paraffin with nitrous oxide, several aspects of the system require refinement to allow better performance characterisation and the potential optimisation.

One of the most critical areas for future work is the integration of an accurate oxidiser mass flow measurement system. The lack of real-time oxidiser flow measurements limited the ability to monitor key performance metrics during the test, such as oxidiser mass flux and O/F ratio. However, post-test weighing of the oxidiser tank provided reliable average values for these parameters, enabling a performance assessment despite the lack of live data. These parameters are essential for correlating regression rate behaviour with operating conditions and to validate theoretical combustion models. The implementation of calibrated flow meters or differential pressure-based measurement systems would significantly improve the fidelity of the experiment.

The observed regression rate of approximately 1.0 mm/s, while within the expected range for paraffin-based systems without regression-enhancing mechanisms, indicates that the engine operated in a relatively low-performance regime. In this test, the maximum recorded chamber pressure was approximately 2.5 bar, which is comparatively low for hybrid rocket operation. Future tests should consider the use of a redesigned nozzle with a smaller throat diameter, which would increase the chamber pressure and, in turn, enhance the convective heat transfer at the fuel surface. As supported by the literature, regression rate in liquefying fuels like paraffin is positively correlated with chamber pressure, particularly when using nitrous oxide as the oxidiser. As chamber pressure increases, the regression rate of paraffin-based fuels initially exhibits a strong positive correlation with pressure due to enhanced convective heat transfer and oxidiser mass flux. However, at higher pressures, typically above 10 bar, a transition occurs where further increases in pressure result in diminishing returns in regression rate. In this regime, the heat transfer from the combustion gases to the fuel surface becomes less dependent on pressure, as the gas boundary layer becomes very thin, and convective heat flux reaches its maximum efficiency. Instead, the regression rate becomes increasingly limited by kinetic factors such as flame speed, fuel surface pyrolysis, and the effectiveness of the oxidiser in promoting surface melting. Additionally, the role of aerodynamic effects, such as turbulent mixing and injector geometry, becomes more pronounced, particularly in systems with highly reactive oxidisers like gaseous oxygen (GOX). As demonstrated in previous studies, in systems utilizing GOX, the regression rate is less sensitive to pressure due to the higher intrinsic reaction rates and the strong dependence of heat feedback on the flow dynamics rather than the chamber pressure itself. This suggests that, beyond a certain threshold, further pressure increases may have minimal impact on performance, and system design should focus more on optimising injector configuration, combustion efficiency, and flow characteristics [39].

In addition to nozzle optimisation, future investigations should consider modifications to injector geometry and the implementation of heat transfer enhancement techniques. Notably, methods such as swirl injection and the incorporation of high-energy additives, such as metal particles like aluminium, require further exploration. The addition of such particles can increase the overall energy density of the fuel and promote secondary combustion phenomena close to the fuel surface. This enhances the convective heat transfer to the fuel surface, hence higher regression rates. This approach has shown boosting in regression rates while also increasing the specific impulse. These strategies have demonstrated efficacy in prior studies, where increased local oxidiser velocity and increased turbulent mixing contributed to an improved entrainment mechanisms and intensified surface melting of the fuel grain.

Further work should also investigate the effect of controlled variation in chamber pressure, supported by proper instrumentation, to establish a more detailed relationship between operating pressure, heat flux, and regression behaviour for the current configuration.

Finally, CFD simulations should be incorporated to better understand internal flow behaviour, heat transfer patterns, and their relationship with the observed uniform regression and wave-like port surface textures, features indicative of early-stage droplet entrainment.

In summary, future developments should prioritise improved diagnostics, nozzle and injector optimisation, and a broader exploration of operating conditions. These efforts will support the advancement of more efficient and scalable hybrid propulsion systems based on paraffin and nitrous oxide.

Bibliography

[1] A. Chandler, E. Jens, B. J. Cantwell, and G. S. Hubbard, “Visualization of the Liquid Layer Combustion of Paraffin Fuel for Hybrid Rocket Applications,” no. August, 2012.

[2] S. S. Mukrimaa *et al.*, *Fundamentals of Hybrid Rocket Combustion and Propulsion*, vol. 6, no. August. 2016.

[3] D. Altman, *Overview and History of Hybrid Rocket Propulsion*. 2007.

[4] G. E. MOORE and K. BERMAN, “A Solid-Liquid Rocket Propellant System,” *J. Jet Propuls.*, vol. 26, no. 11, pp. 965–968, 1956, doi: 10.2514/8.7170.

[5] G. Marxman and M. Gilbert, “Turbulent boundary layer combustion in the hybrid rocket,” *Symp. Combust.*, vol. 9, no. 1, pp. 371–383, 1963, doi: 10.1016/S0082-0784(63)80046-6.

[6] G. A. Marxman, C. E. Wooldridge, and R. J. Muzzy, *Fundamentals of Hybrid Boundary-Layer Combustion*, vol. 15. ACADEMIC PRESS INC., 1964.

[7] K. K. Kuo and M. Chiaverini, *Challenges of Hybrid Rocket Propulsion in the 21st Century*. 2007.

[8] M. V. F. Ribeiro and P. C. G. Junior, “Hybrid Rocket Motors Propellants : A Historical Approach,” *Int. Congr. Mech. Eng.*, no. 21st, pp. 1–15, 2011.

[9] S. T. Of *et al.*, “Aiaa 2003-1162,” no. January, pp. 1–19, 2003.

[10] T. A. Boardman, T. M. Abel, S. E. Claflin, and C. W. Shaeffer, “Design and test planning for a 250-klbf-thrust hybrid rocket motor under the hybrid propulsion demonstration program,” *33rd Jt. Propuls. Conf. Exhib.*, 1997, doi: 10.2514/6.1997-2804.

[11] W. H. Knuth, D. J. Gramer, M. J. Chiaverini, J. A. Sauer, R. H. Whitesides, and R. A. Dill, “Preliminary cfd analysis of the vortex hybrid rocket chamber and nozzle flow field,” *34th AIAA/ASME/SAE/ASEE Jt. Propuls. Conf. Exhib.*, 1998, doi: 10.2514/6.1998-3351.

[12] S. Yuasa, S. Yamamoto, H. Hachiya, K. Kitagawa, and Y. Oowada, “Development of a Small Sounding Hybrid Rocket with a Swirling-Oxidizer-Type Engine,” no. July, 2001.

[13] W. H. Knuth, M. J. Chiaverini, D. J. Gramer, and J. A. Sauer, “Solid-fuel regression rate and combustion behavior of vortex hybrid rocket engines,” *35th Jt. Propuls. Conf. Exhib.*, vol. 18, no. 3, 1999, doi: 10.2514/6.1999-2318.

[14] C. Lee, Y. Na, and G. Lee, “The Enhancement of Regression Rate of Hybrid Rocket Fuel by Helical Grain Configuration and Swirl Flow,” no. July, pp. 1–10, 2005, doi: 10.2514/6.2005-3906.

[15] J. R. Caravella, S. D. Heister, and E. J. Wernimont, “Characterization of fuel regression in a radial flow hybrid rocket,” *J. Propuls. Power*, vol. 14, no. 1, pp. 51–56, 1998, doi: 10.2514/2.5265.

[16] G. A. Risha, E. Boyer, R. B. Wehrman, and K. K. Kuo, “Performance comparison of HTPB-based solid fuels containing nano-sized energetic powder in a cylindrical hybrid rocket motor,” *38th AIAA/ASME/SAE/ASEE Jt. Propuls. Conf. Exhib.*, no. July, 2002, doi:

10.2514/6.2002-3576.

[17] M. Chiaverini, *Review of Solid-Fuel Regression Rate Behavior in Classical and Nonclassical Hybrid Rocket Motors*. 2007.

[18] G. Leccese, “Gas-Surface Interaction, Radiative Heat Transfer and Thermochemistry Modeling in the Simulation of Paraffin-Based Hybrid Rocket Engine,” no. October, 2017.

[19] O. B. George P. Sutton, *Rocket Propulsion Elements*, 8th ed. 2010.

[20] B. Cantwell, A. Karabeyoglu, and D. Altman, “Recent advances in hybrid Propulsion,” *Int. J. Energ. Mater. Chem. Propuls.*, vol. 9, no. 4, pp. 305–326, 2010, doi: 10.1615/IntJEnergeticMaterialsChemProp.v9.i4.20.

[21] R. Theba and C. Bemont, “the Development of a Paraffin Wax/Nitrous Oxide Hybrid Rocket Slab Motor,” no. March, 2019.

[22] B. C. Blount, J. L. Pirkle, J. D. Osterloh, L. Valentin-Blasini, and K. L. Caldwell, “Urinary perchlorate and thyroid hormone levels in adolescent and adult men and women living in the United States,” *Environ. Health Perspect.*, vol. 114, no. 12, pp. 1865–1871, 2006, doi: 10.1289/ehp.9466.

[23] G. Leccese, E. Cavallini, M. Pizzarelli, I. Space, and A. Asi, “State of Art and Current Challenges of the Paraffin – Based Hybrid Rocket Technology,” no. August, 2019, doi: 10.2514/6.2019-4010.

[24] G. A. Marxman, “COMBUSTION IN THE TURBULENT BOUNDARY LAYER ON A VAPORIZING SURFACE,” pp. 1337–1349, 1965.

[25] E. Air, F. Base, P. G. Carrick, and C. W. Larson, “AIAA 95-2948 Lab Scale Test and Evaluation of Cryogenic Solid Hybrid Rocket Fuels Patrick G . Carrick and C . William Larson 31 st AIANASMUSAUASEE Joint Propulsion Conference and Exhibit,” 1995, doi: 10.2514/6.1995-2948.

[26] C. P. St, C. Eric, W. H. Knuth, and D. J. Gramer, “ADVANCED CRYOGENIC SOLID HYBRID ROCKET ENGINE DEVELOPMENTS : CONCEPT AND TEST RESULTS,” 1998, doi: 10.2514/6.1998-3508.

[27] M. E. Derose, K. L. Pfeil, P. G. Carrick, and C. W. Larson, “i AIAA 97-3076 Tube Burner Studies of Cryogenic Solid Combustion Edwards AFB , CA 93524-7680 33rd AlAA / ASME / SAE / ASEEJoint Propulsion Conference & Exhibit,” 1997.

[28] D. J. Gramer, E. E. R. T, W. H. Knuth, and C. P. S. Clair, “EXPERIMENTAL INVESTIGATION OF A METALLIZED CRYOGENIC HYBRID ROCKET ENGINE Daniel J. Gramer*, Eric E. Rice,” 1998.

[29] M. A. (Stanford U. Karabeyoglu, D. (Stanford U. Altman, and B. J. (Stanford U. Cantwell, “Combustion of liquefying hybrid propellants: Part 1, General Theory,” *J. Propuls. Power*, vol. 18, no. 3, pp. 621–630, 2002.

[30] M. A. Karabeyoglu and B. J. Cantwell, “Combustion of Liquefying Hybrid Propellants : Part 2 , Stability of Liquid Films,” vol. 18, no. 3, 2002.

[31] V. I. M. A. A, M. A. Karabeyoglu, B. J. Cantwell, D. Altman, and S. L. City, “DEVELOPMENT AND TESTING OF PARAFFIN-BASED HYBRID ROCKET FUELS,” no. c, 2001.

[32] A. Karabeyoglu, “Scale-Up Tests of High Regression Rate Paraffin-Based Hybrid Rocket Fuels,” no. April 2021, 2004, doi: 10.2514/1.3340.

[33] A. Karabeyoglu, J. Dyer, J. Stevens, and B. Cantwell, “Modeling of N2O Decomposition Events,” no. July, pp. 1–30, 2008, doi: 10.2514/6.2008-4933.

[34] T. Lawrence and J. Sellers, “NITROUS OXIDE AS A ROCKET PROPELLANT,” vol. 48, no. 5, pp. 353–362, 2001.

[35] J. Fonseca, “Refractory ceramics in the context of the fabrication of rocket nozzles : Conventional alumina and industrial waste,” 2023.

[36] B. S. Waxman, “AN INVESTIGATION OF INJECTORS FOR USE WITH HIGH VAPOR PRESSURE PROPELLANTS WITH APPLICATIONS TO HYBRID ROCKETS,” no. June, 2014, [Online]. Available: http://purl.stanford.edu/ng346xh6244%0D.

[37] M. Bouziane, A. E. M. Bertoldi, P. Hendrick, and M. Lefebvre, “Experimental investigation of the axial oxidizer injectors geometry on a 1-kN paraffin-fueled hybrid rocket motor,” *FirePhysChem*, vol. 1, no. 4, pp. 231–243, 2021, doi: 10.1016/j.fpc.2021.11.012.

[38] R. C. Juvinall and K. M. Marshek, *Fundamentals of Machine Component Design*. .

[39] L. Liu, X. He, Y. Wang, Z. Chen, and Q. Guo, “Regression rate of paraffin-based fuels in hybrid rocket motor,” *Aerosp. Sci. Technol.*, vol. 107, p. 106269, 2020, doi: 10.1016/j.ast.2020.106269.

Appendix A

Table 7 - NASA CEA output table.

	Ae/At	Mach	I_{sp}	Pressure	Temperature	Cp	OF
INJECTOR	0.0000E+00	0.0000E+00	0.0000E+00	2.2000E+01	3.2833E+03	3.8736E+00	6.8
COMB END	3.9920E+01	1.4917E-02	1.6412E+01	2.1994E+01	3.2832E+03	3.8736E+00	
THROAT	1.0000E+00	1.0000E+00	1.0610E+03	1.2609E+01	3.0827E+03	3.4937E+00	
EXIT	4.2700E+00	2.6270E+00	2.3265E+03	8.7403E-01	2.0500E+03	1.6090E+00	
INJECTOR	0.0000E+00	0.0000E+00	0.0000E+00	2.3000E+01	3.2875E+03	3.8502E+00	
COMB END	3.9920E+01	1.4917E-02	1.6422E+01	2.2994E+01	3.2874E+03	3.8502E+00	
THROAT	1.0000E+00	1.0000E+00	1.0616E+03	1.3180E+01	3.0859E+03	3.4704E+00	
EXIT	4.2700E+00	2.6283E+00	2.3272E+03	9.1269E-01	2.0490E+03	1.6074E+00	
INJECTOR	0.0000E+00	0.0000E+00	0.0000E+00	2.4000E+01	3.2915E+03	3.8279E+00	
COMB END	3.9920E+01	1.4916E-02	1.6432E+01	2.3994E+01	3.2915E+03	3.8279E+00	
THROAT	1.0000E+00	1.0000E+00	1.0622E+03	1.3751E+01	3.0890E+03	3.4483E+00	
EXIT	4.2700E+00	2.6295E+00	2.3279E+03	9.5132E-01	2.0480E+03	1.6059E+00	
INJECTOR	0.0000E+00	0.0000E+00	0.0000E+00	2.5000E+01	3.2954E+03	3.8066E+00	
COMB END	3.9920E+01	1.4916E-02	1.6441E+01	2.4994E+01	3.2954E+03	3.8066E+00	
THROAT	1.0000E+00	1.0000E+00	1.0628E+03	1.4322E+01	3.0919E+03	3.4272E+00	
EXIT	4.2700E+00	2.6307E+00	2.3286E+03	9.8991E-01	2.0471E+03	1.6045E+00	
INJECTOR	0.0000E+00	0.0000E+00	0.0000E+00	2.6000E+01	3.2991E+03	3.7863E+00	
COMB END	3.9920E+01	1.4916E-02	1.6450E+01	2.5993E+01	3.2991E+03	3.7863E+00	
THROAT	1.0000E+00	1.0000E+00	1.0633E+03	1.4892E+01	3.0948E+03	3.4071E+00	
EXIT	4.2700E+00	2.6318E+00	2.3293E+03	1.0285E+00	2.0463E+03	1.6032E+00	
INJECTOR	0.0000E+00	0.0000E+00	0.0000E+00	2.7000E+01	3.3027E+03	3.7668E+00	
COMB END	3.9920E+01	1.4915E-02	1.6458E+01	2.6993E+01	3.3027E+03	3.7668E+00	
THROAT	1.0000E+00	1.0000E+00	1.0638E+03	1.5463E+01	3.0975E+03	3.3879E+00	
EXIT	4.2700E+00	2.6328E+00	2.3299E+03	1.0670E+00	2.0454E+03	1.6019E+00	
INJECTOR	0.0000E+00	0.0000E+00	0.0000E+00	2.8000E+01	3.3061E+03	3.7482E+00	
COMB END	3.9920E+01	1.4915E-02	1.6466E+01	2.7993E+01	3.3061E+03	3.7481E+00	
THROAT	1.0000E+00	1.0000E+00	1.0643E+03	1.6033E+01	3.1001E+03	3.3694E+00	
EXIT	4.2700E+00	2.6339E+00	2.3305E+03	1.1055E+00	2.0447E+03	1.6008E+00	

Table 8 - Calculations to determine fuel grain dimensions.

Throat Area	A_t	51,5299735	mm^2
Total mass flow rate	$\dot{m}_t$	0,483223943	kg/s
Oxidiser mass flow rate	$\dot{m}_{ox}$	0,42282095	kg/s
Fuel mass flow rate	$\dot{m}_f$	0,060402993	kg/s
Total mass	m_t	2,416119716	kg
Fuel mass	m_f	0,302014965	kg
Oxidiser mass	m_{ox}	2,114104752	kg
Volume of fuel	V_f	335572,1828	mm^3
Area of fuel	A_f	22371,47886	mm^2

Code used in the data acquisition and ignition control systems:

Data acquisition system (DAS):

```
#include <HX711_ADC.h>
#include <RH_RF95.h>
#include <SPI.h>
#include <SoftwareSerial.h>
#include "SdFat.h"

// Definitions for the SD and SPI
#if SPI_DRIVER_SELECT == 2  // Ensure this is set in SdFat/SdFatConfig.h

#define SD_FAT_TYPE 1  // Assuming FAT32 formatted SD card
const uint8_t SD_CS_PIN = 33;
const uint8_t SOFT_MISO_PIN = 39;
const uint8_t SOFT_MOSI_PIN = 35;
const uint8_t SOFT_SCK_PIN = 37;

SoftSpiDriver<SOFT_MISO_PIN, SOFT_MOSI_PIN, SOFT_SCK_PIN> softSpi;
#define SD_CONFIG SdSpiConfig(SD_CS_PIN, SHARED_SPI, SD_SCK_MHZ(0), &softSpi)

SdFat32 sd;
File32 file;

// LoRa and Load Cell settings
#ifdef __AVR__
#define COMSerial mySerial
#define ShowSerial Serial
SoftwareSerial mySerial(51, 53);  // 51 (RX) and 53 (TX)
RH_RF95<SoftwareSerial> rf95(COMSerial);
#endif

#define HX711_ADC_config_h
const int HX711_dout_1 = 5;
const int HX711_sck_1 = 4;
const int HX711_dout_2 = 3;
const int HX711_sck_2 = 2;
const int relayPin1 = 47;  // First relay pin
const int relayPin2 = 45;  // Second relay pin
int pressao = A0;
float Vref = 5.13;
float calibrationValue_1 = 144663;
float calibrationValue_2 = -21760;

HX711_ADC LoadCell_1(HX711_dout_1, HX711_sck_1);
HX711_ADC LoadCell_2(HX711_dout_2, HX711_sck_2);
unsigned long t = 0;

void logToFile(const String& message) {
  if (file.open("data.txt", O_RDWR | O_CREAT | O_AT_END)) {
    file.println(message);
    file.close();
```

```
  } else {
    ShowSerial.println("Failed to open file for writing");
  }
}

void setup() {
  ShowSerial.begin(9600);
  delay(10);
  ShowSerial.println("Starting...");

  COMSerial.begin(9600);

  if (!rf95.init()) {
    ShowSerial.println("Start failed");
    while (1);
  } else {
    ShowSerial.println("Ready");
  }

  if (!rf95.setFrequency(434.0)) {
    ShowSerial.println("setF failed");
  } else {
    ShowSerial.println("setF success");
  }

  pinMode(relayPin1, OUTPUT);
  pinMode(relayPin2, OUTPUT);
  digitalWrite(relayPin1, HIGH);
  digitalWrite(relayPin2, HIGH);

  pinMode(pressao, INPUT);

  LoadCell_1.begin();
  LoadCell_2.begin();
  LoadCell_1.start(1000, true);
  LoadCell_2.start(1000, true);
  LoadCell_1.setCalFactor(calibrationValue_1);
  LoadCell_2.setCalFactor(calibrationValue_2);

  if (!sd.begin(SD_CONFIG)) {
    Serial.print("begin() failed\n");
    if (sd.card()->errorCode()) {
      sd.printSdError(&Serial);
    }
    return;
  }

  logToFile("Starting data logging...");
}

void loop() {
  const int relay1_time = 5000;
```

```
const int relay2_first_delay = 4000;
const int relay2_first_time = 500;
const int relay2_break_time = 2000;
const int relay2_second_time = 5000;

static bool relay1Active = false;
static bool relay2FirstActive = false;
static bool relay2SecondPending = false;
static bool relay2SecondActive = false;
static bool relay2FirstDeactivated = false;

static unsigned long relay1StartTime = 0;
static unsigned long relay2FirstStartTime = 0;
static unsigned long relay2SecondStartTime = 0;

// Handle incoming LoRa messages
if (rf95.available()) {
  uint8_t buf[RH_RF95_MAX_MESSAGE_LEN];
  uint8_t len = sizeof(buf);

  if (rf95.recv(buf, &len)) {
    String receivedMessage = String((char*)buf);

    if (receivedMessage == "ignition") {
      ShowSerial.println("Ignition message received");
      logToFile("Ignition message received");

      relay1StartTime = millis();
      digitalWrite(relayPin1, LOW);
      relay1Active = true;

      relay2FirstStartTime = millis() + relay2_first_delay;
      relay2FirstActive = true;
    }
  }
}

// Relay timing logic
if (relay1Active && millis() > relay1StartTime + relay1_time) {
  digitalWrite(relayPin1, HIGH);
  relay1Active = false;
  ShowSerial.println("Relay 1 stopped.");
  logToFile("Relay 1 stopped.");
}

if (relay2FirstActive && millis() > relay2FirstStartTime) {
  digitalWrite(relayPin2, LOW);
  relay2FirstStartTime = millis();
  relay2FirstActive = false;
  relay2SecondPending = true;
  relay2SecondStartTime = millis() + relay2_first_time + relay2_break_time;
  ShowSerial.println("Relay 2 first activation (0.5 sec).");
```

```
    logToFile("Relay 2 first activation (0.5 sec).");
  }

  if (!relay2FirstActive && relay2SecondPending && !relay2FirstDeactivated && millis() > relay2FirstStartTime + relay2_first_time) {
    digitalWrite(relayPin2, HIGH);
    relay2FirstDeactivated = true;
  }

  if (relay2SecondPending && millis() > relay2SecondStartTime) {
    digitalWrite(relayPin2, LOW);
    relay2SecondPending = false;
    relay2SecondActive = true;
    relay2SecondStartTime = millis();
    ShowSerial.println("Relay 2 second activation (5 sec).");
    logToFile("Relay 2 second activation (5 sec).");
  }

  if (relay2SecondActive && millis() > relay2SecondStartTime + relay2_second_time) {
    digitalWrite(relayPin2, HIGH);
    relay2SecondActive = false;
    ShowSerial.println("Relay 2 second deactivation.");
    logToFile("Relay 2 second deactivation.");
  }

  // Sensor Data Logging
  if (LoadCell_1.update() && LoadCell_2.update()) {
    if (millis() > t + 500) {
      float data[3];
      data[0] = LoadCell_1.getData();
      float b = analogRead(pressao);
      data[1] = (34.47 - 0.0) / (4.5 - 0.5) * (b * Vref / 1023 - 0.5);
      data[2] = LoadCell_2.getData();

      float dataToSend[] = {data[1], data[2]};
      rf95.send((uint8_t*)dataToSend, sizeof(dataToSend));
      rf95.waitPacketSent();

      logToFile("LC1Tank mass: " + String(data[0], 3) + " kg | Pressure: " + String(data[1], 3) + " bar | LC2Thrust: " + String(data[2], 3) + " kg | Time: " + String(millis()));
      t = millis();
    }
  }
}

#endif  // SPI_DRIVER_SELECT
```

Ignition control system (ICS):

```
#include <SPI.h>
#include <RH_RF95.h>
```

```
#ifdef __AVR__
#include <SoftwareSerial.h>
SoftwareSerial SSerial(5, 6); // RX, TX
#define COMSerial SSerial
#define ShowSerial Serial
RH_RF95<SoftwareSerial> rf95(COMSerial);
#endif

void setup() {
  ShowSerial.begin(9600);
  delay(10);
  ShowSerial.println("Starting...");

  if (!rf95.init()) {
    ShowSerial.println("Start failed");
    while (1);
  } else {
    ShowSerial.println("Ready");
  }

  if (!rf95.setFrequency(434.0)) {
    ShowSerial.println("setF failed");
  } else {
    ShowSerial.println("setF success");
  }
}

void loop() {
  // Handle commands sent via Serial
  if (ShowSerial.available()) {
    String command = ShowSerial.readStringUntil('\n');
    command.trim();

    if (command == "ignition") {
      uint8_t code[] = "ignition"; // Code message for ignition
      rf95.send(code, sizeof(code));
      rf95.waitPacketSent(); // Ensure the packet is fully sent
      ShowSerial.println("Ignition message sent");
    } else if (command == "stop") {
      uint8_t code[] = "stop"; // Code message for stop
      rf95.send(code, sizeof(code));
      rf95.waitPacketSent(); // Ensure the packet is fully sent
      ShowSerial.println("Stop message sent");
    } else {
      ShowSerial.println("Unknown command. Use 'ignition' or 'stop'.");
    }
  }

  // Check for received messages
  if (rf95.available()) {
    uint8_t buf[RH_RF95_MAX_MESSAGE_LEN];
    uint8_t len = sizeof(buf);
```

```
    if (rf95.recv(buf, &len)) {
      float a = *((float*)&buf[0]);
      float b = *((float*)&buf[4]);
      ShowSerial.print("Received: ");
      ShowSerial.print(a);
      ShowSerial.print(" bar | ");
      ShowSerial.print(b);
      ShowSerial.println(" kg ");

      // Wait 1 second before processing the next received value
      delay(1000);
    } else {
      ShowSerial.println("recv failed");
    }
  } else {
    // Print "Waiting" every 10 seconds when no data is being received
    static unsigned long lastWaitMessage = 0;
    if (millis() - lastWaitMessage >= 10000) {
      ShowSerial.println("Waiting");
      lastWaitMessage = millis();
    }
  }
}
```